UNIVERSITÀ DEGLI STUDI DI TRIESTE

UNIVERSITÀ DEGLI STUDI DI TRIESTE

XXXIV CICLO DEL DOTTORATO DI RICERCA IN

Ingegneria Industriale e dell'Informazione
Curriculum Ingegneria Meccanica, Navale, dell'Energia e della Produzione

A Combined FEM-CFD Methodology to Study and Optimize Acoustic Properties of Marine Exhaust Lines

Settore scientifico-disciplinare: **ING-IND/02**, ING-IND/01, ING-IND/27

DOTTORANDA
Giada Kyaw Oo D'Amore

COORDINATORE
Prof. Alberto Tessarolo

SUPERVISORE DI TESI
Prof. Marco Biot

CO-SUPERVISORI DI TESI
Prof. Mitja Morgut

Prof. Jan Kašpar

PhD Francesco Mauro

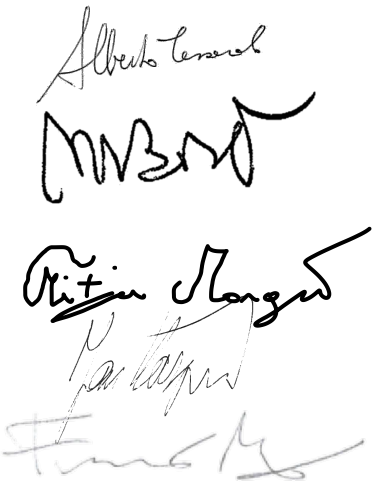

ANNO ACCADEMICO 2020/2021

Come sempre a mio nonno,
ma questa volta ancor di più a mio papà…
mi manchi.
Un brindisi a voi lassù,
spero siate orgogliosi di me!

Contents

Introduction

Maritime transport is of great importance for the global economy, as it accounts for around 80% of worldwide trade, together with its related activities (e.g., shipbuilding, repairs, ports activities) [1]. Due to the extensive use of heavy fuel oils, maritime transport accounts for approximately 10-15% of global Sulphur (SOx) and Nitrogen Oxides (NOx) emissions. This led to an increasing concern about the global impact of maritime emissions. IMO (International Maritime Organization), consistently, has restricted the limits imposed by MARPOL 73/78 Annex VI Regulation [2] on ships emissions. The more restrictive limits are imposed on SOx and NOx emissions (Figure 1) for special restricted areas, i.e. SECAs (Sulfur Emission Control Areas) and ECAs (Emission Control Areas) (Figure 2) [2].

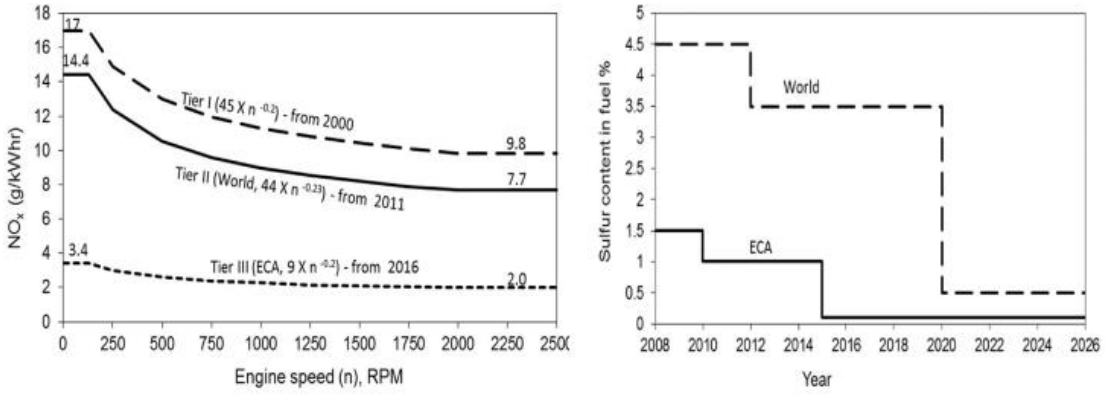

Figure 1: NOx and SOx limits.

Figure 2: ECAs.

Introduction

EGR (Exhaust Gas Recirculation) and SCR (Selective Catalytic Reduction) systems are effective technologies for the control of marine NOx emissions [3,4]. However, the former solution increases particulate matter emissions and fuel consumption by about 4% [5], making SCR the preferred option.

Different strategies allow for reducing SOx emissions [6]: alternative fuels (e.g. LNG-Liquefied Natural Gas), alternative energy sources (e.g. fuel cell) and conventional fuels with low Sulphur content (e.g. VLSFO-Very Low Sulphur Fuel Oil). Since January 2020, the above-quoted Regulations made VLSFO mandatory for ships employing conventional fuels, as its Sulphur content is lower than 0.5 wt%. Moreover, to sail in the SECAs, ULSFO (Ultra Low Sulphur Fuel Oil) must be used as the Sulphur content limit in fuels was pushed down to 0.1 wt% in these areas. Whereas the adoption of alternative fuels or onboard energy sources represents, besides the costs, the burden of the entire propulsion system refitting, low Sulphur content combustibles significantly impact the total ship operating costs, being over 60% of them associated with the fuel. The Rotterdam/Antwerp hub on February 22nd, 2021 [7] reports prices of $365, $472, $515, $520 per ton for respectively HSFO (High Sulphur Fuel Oil), VLSFO, ULSFO, MGO (Marine Gas Oil), indicating that use of HSFO may represent a higher saving compared to the other fuels. These values increased respectively to $657, $898, $1065 and $1317 as of June 3rd, 2022 further highlighting the impact of the fuel cost on shipping [8]. Accordingly, an alternative solution is the installation of scrubbers as an Exhaust Gas Cleaning Systems (EGCS) to ensure compliance with SOx regulation. Scrubbers represent a viable solution [9] and show a lower climate impact than low Sulphur fuels [10]. This aspect is confirmed also by EGCS manufacturers, asserting that the costs saved by using HSFO instead of LSFO can pay back the costs of installing and operating EGCS in about one year [11].

The installation of both SCR and scrubber systems onboard could represent a reliable technical solution to satisfy the limits imposed on both the NOx and SOx emissions. However, those solutions are hardly applicable because of space limitations, especially for existing ships [12]. Indeed, the pollution control devices are usually installed in the funnel and have a large size, so integrating such systems with other components of the exhaust line, like silencers, becomes mandatory to save space [3].

Ships emissions are not limited to chemical pollution, but remarkable is also the importance of controlling and minimizing the exhaust gas noise. Several regulations and

class notations [13–15] limit the perceived noise level at the ship's decks and prescribed distances from the vessels, both during the navigation and during the stay in ports.

So, the integration between pollution control devices and silencers can represent a smart way to satisfy the regulations: system integration lead to space-saving along the exhaust line, allowing the installation of scrubbers.

Prototypes of integrated SCRs-silencers have been already constructed [16], but in literature only a few studies of the acoustic performances of SCRs are reported [3,17], while for scrubbers systems no research could be found that evaluates these characteristics.

On the contrary, acoustic performances of silencers/mufflers were reported extensively, especially in the automotive industry [18–22]. The acoustic properties of such system are usually study using both the FEM [23–25] and CFD [26–29] approaches; the first one considers the geometry as an influencing parameter, while the second one takes into account also the influence of the flow inside the silencer and allows to evaluate the pressure drop generated by the analyzed system. However, the CFD approach requires a high computational cost and more complicated modelling. Just a few works in literature propose a combined approach between FEM and CFD [21,30], that allows for reducing the computational burden of full CFD modelling. However, those works use simplified models that, for example, do not consider the viscous dissipations in the acoustic simulations. As a matter of fact, the use of a numerical model leads to saves in terms of both time and costs for the optimization of the flow field along the exhaust line, and the number of prototypes to be constructed and tested can be significantly reduced.

Thesis scope and objectives

As above reported, development of compact abatement systems capable of reducing both NOx and SOx is of strong interest, due to the difficulty of combining both SCR and scrubber technologies on a ship [12]. This is one of the objectives of the project ABE[1], which addresses the problem of simultaneous NOx and SOx abatement by using a combination of a Diesel Oxidation Catalyst (DOC), which promotes oxidation of NO and hence its solubility, followed by a closed-loop scrubber. A pilot demonstrator has been constructed at the University, which acoustic properties are studied and modelled in the present project.

The scope of this thesis comes from the need for system integration along the exhaust line to save space and the need to have a proper numerical model to simulate the acoustic properties of ECGs for their optimization. Therefore, the main objectives of the thesis can be summarized in the following points:

1. develop a robust and computationally-efficient numerical methodology to study acoustic properties of exhaust line components;
2. combine CFD and FEM simulations to capture the influence of the flow on the acoustic properties, while keeping a reasonably low computational time;
3. optimize the acoustic properties of exhaust line components, while respecting the constraints imposed on both geometrical parameters and flow characteristics by the chemical reactions needed to satisfy NOx and SOx regulations.

Figure 3 shows a flow chart outlining the calculation framework employed in this study.

[1] ABE-Abbattimento delle emissioni vibroacustiche e chimiche in ambito navale" project funded by Regione Autonoma Friuli Venezia Giulia, POR-FESR 2014–2020, attività 1.3b Incentivi per progetti di R&S da realizzare attraverso partenariati pubblico privati nelle aree di specializzazione Tecnologie Marittime e Smart Health—DGR 849/16.

Scope of the thesis

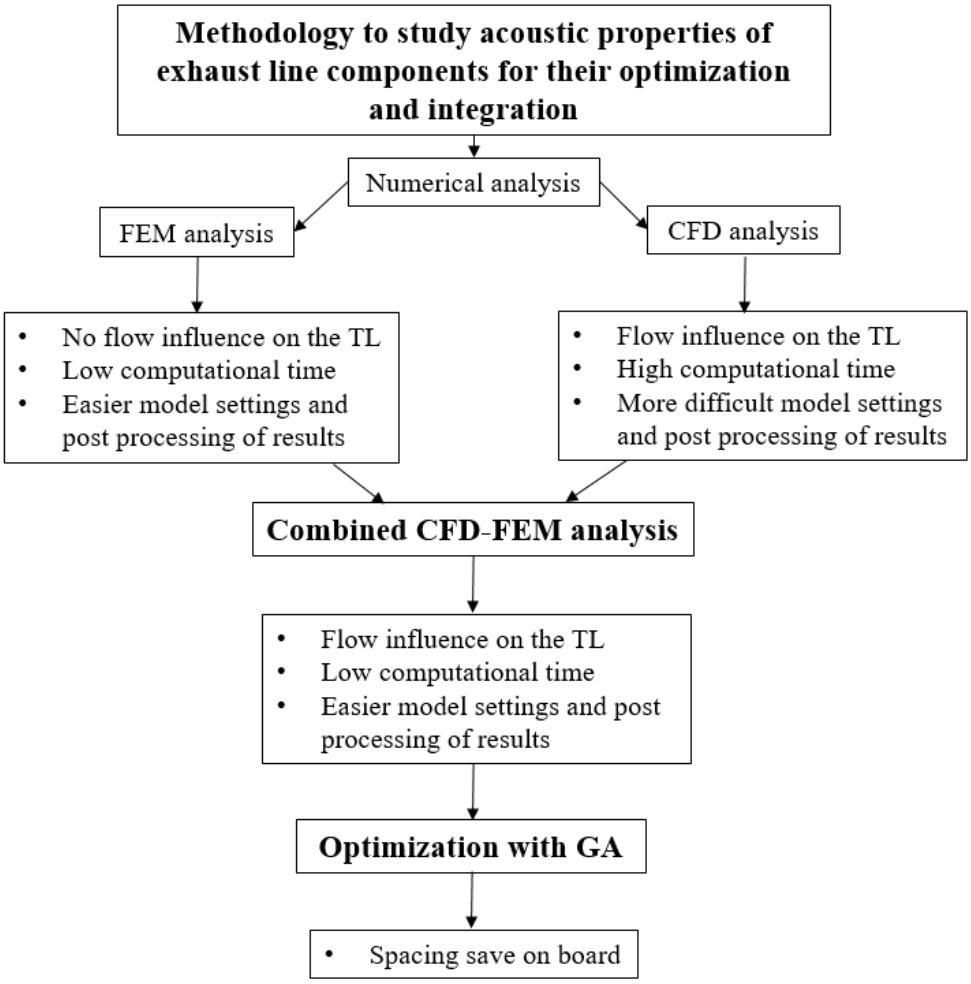

Figure 3: Flow chart of the novel calculation framework for acoustic properties on exhaust lines.

Some preliminary studies are performed to optimize computational effort of numerical simulations. Moreover, experimental measurements are performed on both a simplified set-up (impedance tube) and a mockup of a marine Genset exhaust line in order to assess the numerical results.

The assessed CFD and FEM simulations are used for the combined approach that, firstly, calculates the flow field (velocity and temperature) with a steady-state CFD simulation and, then, imports this field into the acoustic FEM model through mesh mapping to evaluate the Transmission Loss (TL) of the studied geometry in presence of flow. Figure 4 provides a schematic representation of the simulations and experimental measurements performed within the study.

Scope of the thesis

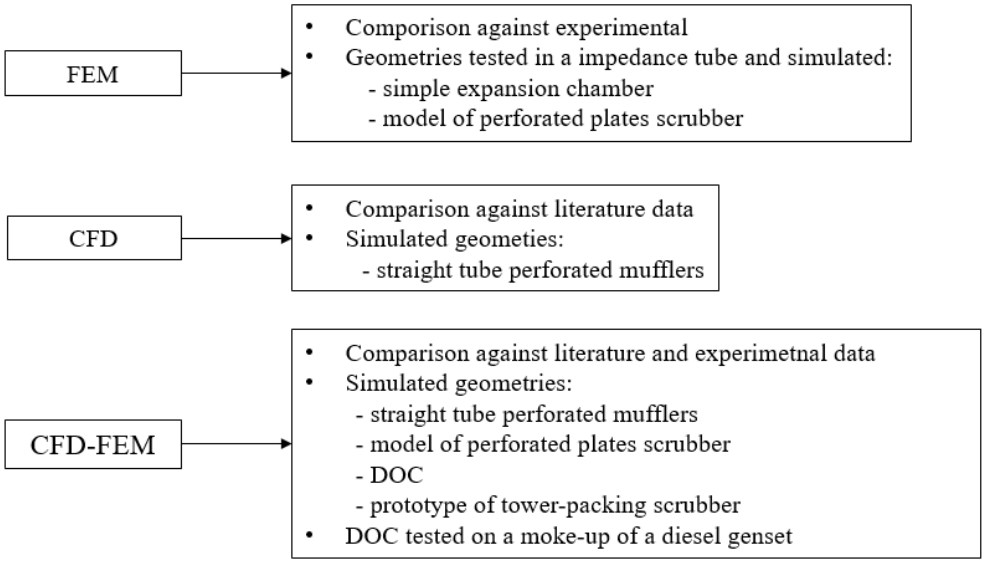

Figure 4: Schematic representation of experimental tests and simulations.

The combined approach is then used on real systems, to assess and model the acoustics properties of both DOC and scrubber constructed - within the ABE project - for the Genset mockup as an advanced exhaust abatement system. Their TL reach values up to 60 dB, which allows elimination of the traditional silencer, thus reducing the overall dimensions. In this manuscript a general overview on NOx and SOx abatement system mostly used on board ships is reported in Chapter 1. Then a hint of theory on method to experimentally measure the TL of silencers is addressed in Chapter 2. Chapter 3 contains an overview on the numerical approaches used in this research, explaining how they work, their boundary conditions and how they model components such as perforated pipes and plates and catalysts. The application of the proposed numerical methodology (combined CFD-FEM) to different case study is reported in Chapter 4, which also comprehends the optimization process developed to optimize the acoustic properties of the analyzed ECGs. Conclusion and future developments are reported in Chapter 5. The preliminary studies performed to assess the FEM and CFD model are reported in Appendix, those represents already published works. Also the illustration of experimental set-ups (impedance tube and Genset mockup) and measurements is addressed in Appendix.

Chapter 1

The Marine Pollution Abatement Systems

This chapter gives a brief description of the geometry and operation of the abatement systems typically used onboard, for both acoustic and chemical emissions.

1. SCRs (Selective Catalytic Reduction)

SCRs are widely used onboard to reduce the NOx emissions from marine diesel engine, that are generated by the high temperatures in the combustion chamber.

Those systems include the injection of a urea solution into the exhaust line where the exhaust gas heat is used to produce ammonia (NH_3). This then selectively reduces NOx on a catalyst, reducing NOx into harmless nitrogen and water. In Figure 5 a scheme of urea water spry and the catalyst is reported: the catalyst is in the form of a monolith made by sheets of materials (ceramic or metallic) that form channels of different shapes (e.g. squared, sinusoidal, …) through which the exhausts flow. The monoliths are characterized by the number of cells per square inch (CPSI), as well as by the material, channel geometry and open area. As a result, there is a specific pressure drop across the monolith which is a function of exhaust conditions (flow-rate, temperature, pressure, etc.). In principle, higher is the value of CPSI, *i.e.* catalyst exposed area, and higher would be the degree of NOx abatement, yet the pressure drop across the monolith and the facility of clogging with narrow channels represents severe limitations. Accordingly, a compromise has to be adopted in order to not negatively influence the engine efficiency while keeping the NOx abatement compliant with regulations.

According to the type of catalyst, e.g. SCR , DOC or Three-way catalyst (TWC) used in the automotive sector [31], the catalytically active formulation is deposited as a thin layer over the surface of the channels of the honeycomb monoliths; alternatively, the monolith can be made of the catalysts itself when the catalytic formulations is suitable for being subjected to an extrusion process and the process is economically viable. This is the case, for example, for some V_2O_5-WO_3-TiO_2-based SCR catalysts [32]. Important is to underline that for all of the catalysts considered, i.e., SCR, DOC of TWC, the monolith geometry is common as it is dictated, as above reported, by the requirement to optimize the flow-rate / backpressure ratio, in addition to other factors.

SCR can operate as a standalone technology (not requiring any additional devices) and is able to reduce NOx by 80% or more. Its installation does not require significant engine modifications, but the storage of urea, the injection system and the catalyst take huge space onboard and along the exhaust line.

There are different SCR catalyst monoliths available, with different chemical formulations and shapes. In the case of marine engines, which use fuel with high sulfur concentration, vanadium-based catalysts are usually used because of their appreciable resistance to sulfur poisoning. In this regard, exists a relationship between fuel sulfur concentration and exhaust gas temperature where acidic ammonium sulfate precipitation occurs: the acidic ammonium sulfate clogs the catalyst and lowers the NOx reduction rate, so it is necessary to keep the exhaust gas at an appropriate temperature [33–36].

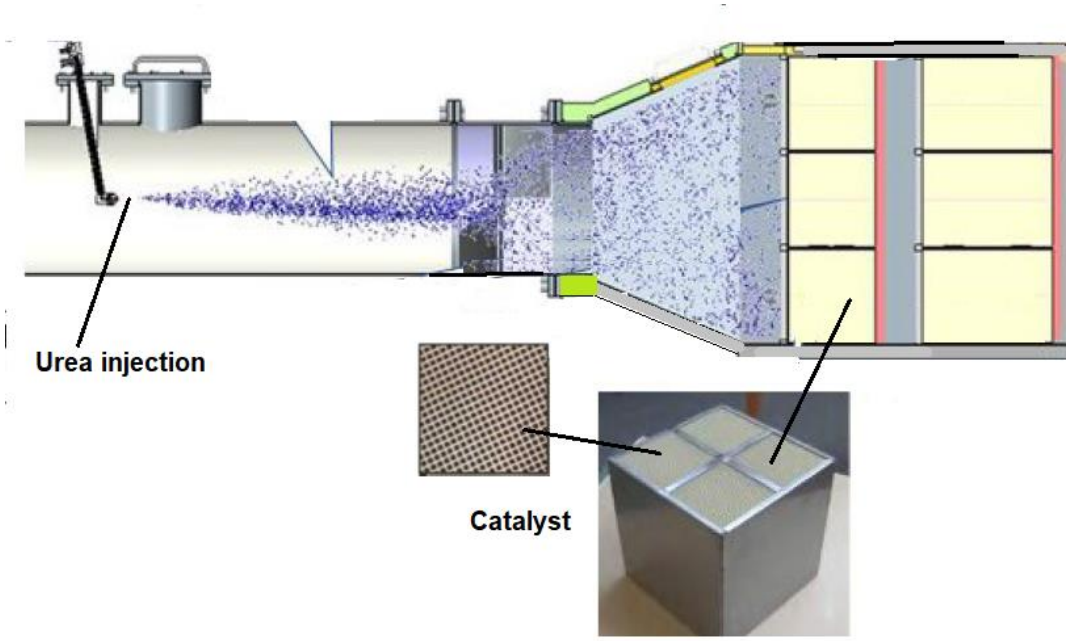

Figure 5: SCR components. (Figure adapted from **[37]**)

2. Scrubber Systems

Scrubber systems are used onboard ships for the abatement of SOx while using fuels with high sulfur content. Scrubbers can use two main type of operation: dry scrubbers utilize a chemical adsorption process that trap the sulfur dioxide (SO_2) by converting it into a stable compound; wet scrubbers mix the exhaust gas with wash water sprayed in counter flow and the water soluble components of the exhaust gas are removed by dissolution into the wash water [38].

Wet scrubbers are mostly used on board ships as they have a higher efficiency being able to remove SOx up to 95% from exhaust gas. By removing SOx from the exhaust, the scrubber also removes most of the direct sulphate particulate matter (PM) and controls much of the secondary PM that is formed in the atmosphere from these emissions. As a matter of fact, Sulphates are a large portion of the PM from ships operating with high sulphur fuels [39]. Moreover, the removal of ultrafine particles produced by diesel engines appears to be more effectively achieved at lower temperatures created by wet scrubbers. The wet scrubber can also raise the rate of NO_x abatement as some nitrogen oxides are highly water-soluble [38].

There are two main types of wet scrubber technologies. The first wet scrubber technology, referred to as seawater scrubbing, is an open-loop design which uses seawater to scrub the exhaust before discharging the wash water back to the sea following treatment (Figure 6). The SO_2 and SO_3 in the exhaust gas dissolves in the wash water, the natural alkalinity of the seawater is used to neutralize the acidity that results from SOx removal. Wash water is then treated to remove solids and raise the proper pH prior to discharge back to sea. The removed solids are stored onboard for shore-side disposal.

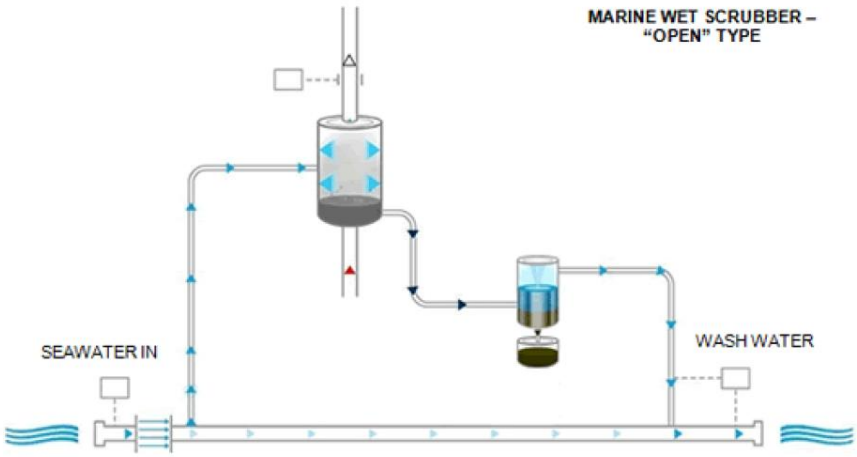

Figure 6: Marine wet scrubber: open type. (Figure adapted from [40])

The second one is a closed-loop system (Figure 7). Freshwater is used as wash water and an alkali-containing consumable additive (normally caustic soda) is injected into the wash water to favor absorption and neutralization of the sulfur oxides contained in the exhaust. Wash water is recirculated and any evaporative loss is replaced with additional freshwater. Typically, closed freshwater systems have much smaller discharge rates than seawater scrubbers and treat a smaller volume of effluent.

Freshwater scrubbers are used when high-efficiency cleaning is needed (greater than 90%) or when low-alkalinity seawaters, e,g, the Baltic sea, preclude the use of seawater scrubbers. The ability to operate an EGCS without discharging wash water for short periods of available holding tank capacity may be advantageous in water bodies that are especially sensitive or vulnerable, such as enclosed water bodies and/or those with low alkalinity [39].

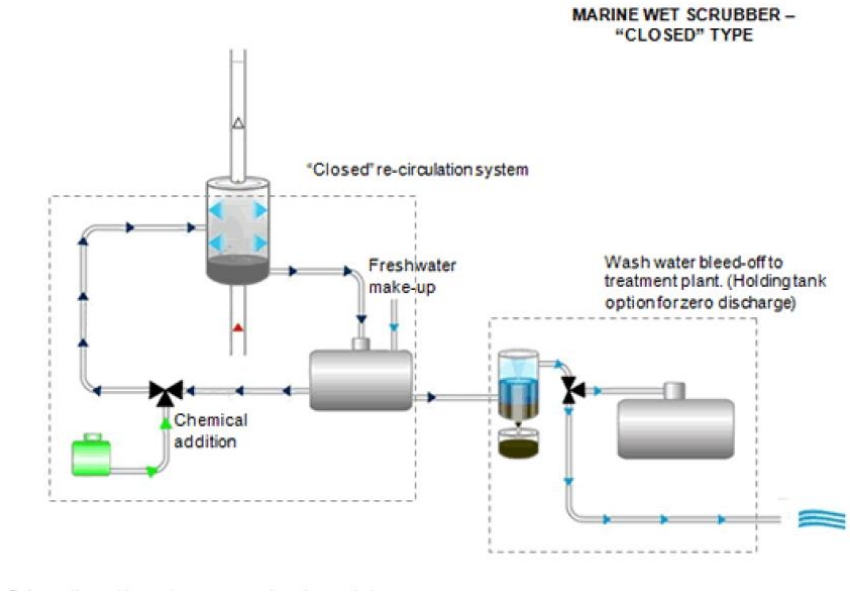

Figure 7: Marine wet scrubber: closed type. (Figure adapted from [40])

There are numerous configurations of scrubbing systems, all designed to provide good contact between the liquid and dirty gas. The most used on boards ships is the packed towers scrubber shown in Figure 8. The exhaust gas enters the bottom of the tower and flows upward over the packing material. The liquid is sprayed at the top of the packing and it flows down over the packing material. As the exhaust stream moves up through the packing, it is forced to make many tortuous changes in direction, resulting in the intimate mixing of both the exhaust gas and liquid streams. The packing is constituted of different layers, each one made of corrugated sheets welded together to form channels of a certain shape and size and inclined at a certain angle (Figure 9). At the top of the tower, a mist eliminator is used to remove water droplets from the exhaust [39].

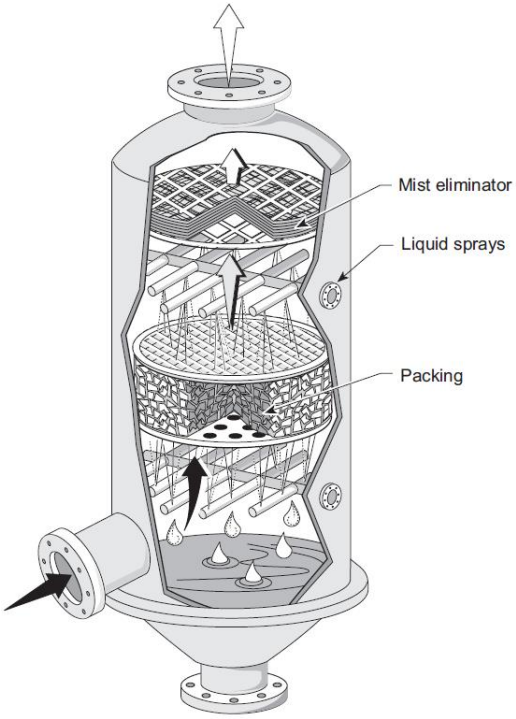

Figure 8: Packed tower wet scrubber. (Figure adapted from **[39]**)

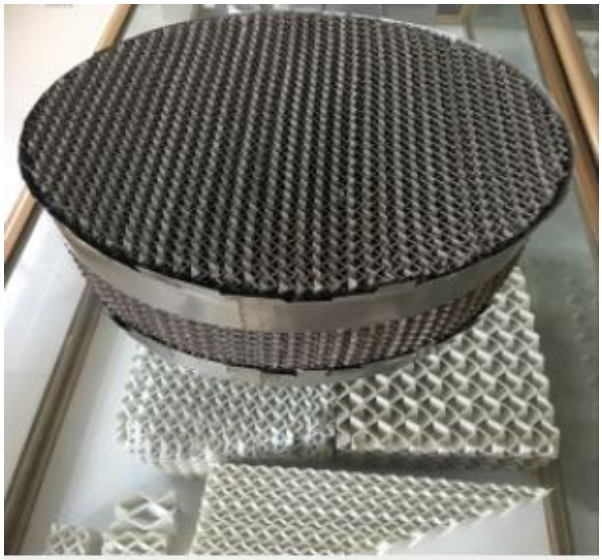

Figure 9: Example of tower packing layer.

3. Silencers

A silencer is a device used in a flow duct to prevent sound from reaching the openings of the duct and radiating as far-field noise. It is a necessary component used in the design of any exhaust for internal combustion engines. There are three basic requirements for a

modern exhaust system: compact outer geometry, sufficient attenuation, and low-pressure drop.

Two different physical principles are used for sound reduction in silencers. Sound can be attenuated by the use of sound-absorbing materials in which sound energy is converted into heat mainly by viscous processes (Figure 10). These types of silencers are called absorptive. Typical sound-absorbing materials used are rock wool, glass wool, and plastic foams. To force the exhaust flow through the absorbing material would create a large pressure drop so the material is usually placed concentrically around the main exhaust pipe. To protect the absorbing material and prevent it from being swept away by the flow, a perforated pipe is usually inserted between the main pipe and the absorbing material. Sometimes a thin layer of steel wool is included for additional protection.

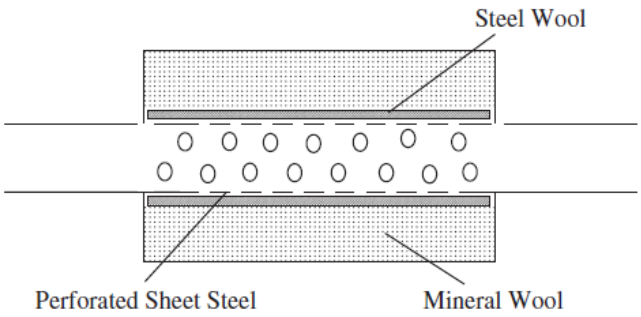

Figure 10: Absorptive silencer, typical configuration. (Figure adapted from **[41]**)

The other physical principle reaches the attenuation through the reflection of sound, which is caused by area changes or the use of different kinds of acoustic resonators (Figure 11). These types of silencers are called reactive. When the acoustic energy is reflected toward the source, multiple reflections between the source and the reactive silencer can occur, as the source is not reflection-free, leading to an increase in sound pressure levels. So the reactive silencer should be properly designed and used to cause a mismatch in the acoustic properties of the exhaust system and the source to reduce the acoustic energy generated by the source.

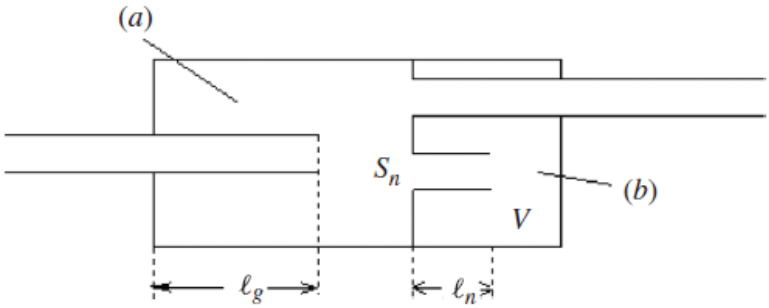

Figure 11: Example of a reactive silencer. (Figure adapted from **[41]**)

There are also cases where resistive and reactive properties are combined in the same silencer element. All reactive silencer elements can cause some loss of acoustic energy in addition to reflecting a significant part of the acoustic energy toward the source. The losses can be increased, for instance, by using perforated elements and reducing the hole size of perforation, especially if the flow is forced through the holes. Figure 12 shows some typical perforate silencer elements, where especially the cross-flow and reverse-flow types have a significant resistive as well as a reactive character [41,42].

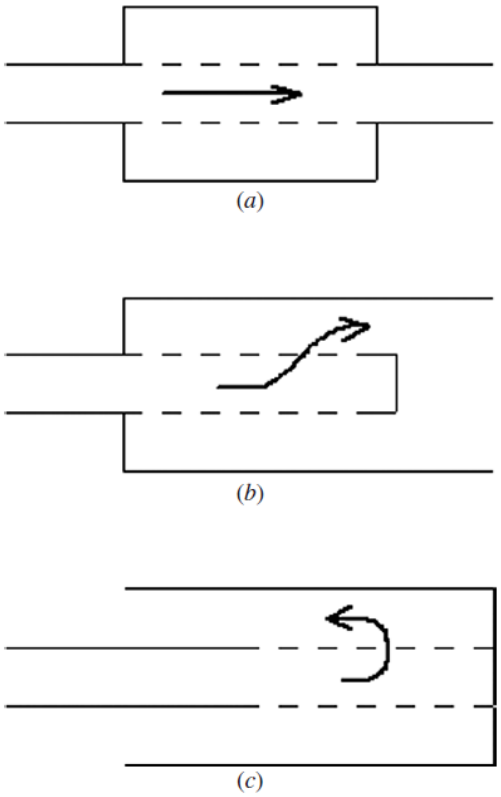

Figure 12: Different types of perforated muffler elements having both reactive and resistive character: (a) through flow, (b) cross flow, and (c) reverse flow. (Figure adapted from [41])

Several parameters describe the acoustic performance of a silencer and/or its associated piping. These include noise reduction (NR), insertion loss (IL), and transmission loss (TL). The NR is the sound pressure level difference across the silencer. Though the NR can be easily measured, it is not particularly helpful for silencer design. The IL is the sound pressure level difference at a point, usually outside the system, without and with the silencer present. Though the IL is very useful to the industry, it is not so easy to calculate since it depends not only on the silencer geometry itself but also on the source impedance and the radiation impedance. The TL is the difference in the sound power level between the incident wave entering and the transmitted wave exiting the silencer when the silencer termination is anechoic. The TL is a property of the silencer only and can be easily calculated from both analytical and numerical models but is difficult to measure [19]. Some experimental methodology for its evaluation is reported in the literature, in the next chapter, a summary of these measurements set-up is addressed.

Chapter 2

Measurement techniques for TL evaluation

In general, the TL of a component can be calculated with the following equation, considering an anechoic termination [43]:

$$TL = 10log_{10} {}^{W_i}/_{W_t} \quad \text{Eq. 1}$$

where W_i and W_t are the incidents and the transmitted waves' sound power respectively. Three distinct techniques allow measuring TL for silencers using an impedance tube: the decomposition method, the two-sources method and the two-loads method.

The decomposition method [44,45] measures acoustic properties in-ducts using a measurement set-up as depicted in Figure 13. S_{ii}, S_{rr}, and S_{tt} represent the auto-spectra of the incident, reflected and transmitted sound waves, respectively.

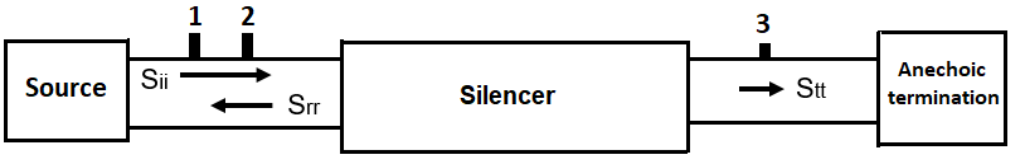

Figure 13. Measurement set-up according to the decomposition theory.

Considering a plane wave propagation and using two microphones at locations 1 and 2, the sound pressure can be decomposed into its incident and reflected waves. The microphone at location 3 directly measures the transmitted sound pressure as the anechoic termination avoids reflection. The decomposition theory provides an expression for the auto-spectrum S_{ii} of the incident wave, so the sound power of incident and transmitted waves can be derived and the TL can be expressed as follows [19]:

$$TL = 20log_{10} {}^{p_i}/_{p_t} + 10log_{10} {}^{S_i}/_{S_o} \quad \text{Eq. 2}$$

where p_i and p_t are the RMS (Root Mean Square) pressure amplitude of the incident and transmitted sound waves respectively, and S_i and S_o are the cross-section area of silencer inlet and outlet pipe respectively.

The major drawback of the decomposition method is that a fully anechoic termination is difficult to reproduce in experiments, affecting the reliability of the TL measurement.
A silencer can also be modelled using the so-called four-pole parameters method [42]. The four parameters (*A*, *B*, *C* and *D*) relate the inlet pressure (p_i) and velocity (v_i) to respective outlet values (p_o, v_o), assuming a plane wave propagation, as expressed in the following equation:

$$\begin{bmatrix} p_i \\ v_i \end{bmatrix} = \begin{bmatrix} A & B \\ C & D \end{bmatrix} \begin{bmatrix} p_o \\ v_o \end{bmatrix} \quad \text{Eq. 3}$$

Two methods are available to calculate the four-pole parameters exploiting the transfer-matrix approach: the two-sources method and the two-loads method [19].
When using the two-sources method, four microphones are needed, and the sound source position has to be changed, as shown in Figure 14.

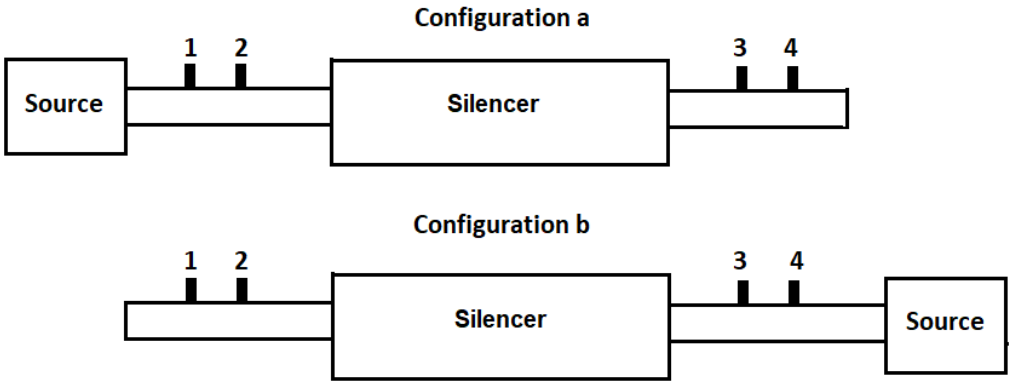

Figure 14. Measurement set-up according to the two-source method.

The silencer TL can be calculated as follows [19,46]:

$$TL = 20log_{10}\left\{{}^{1}/_{2}\left|A_{23} + {}^{B_{23}}/_{\rho c} + \rho c\, C_{23} + D_{23}\right|\right\} + 10log_{10}\,{}^{S_i}/_{S_o} \quad \text{Eq. 4}$$

where ρ is the fluid density, c is the speed of sound in the fluid medium and A_{23}, B_{23}, C_{23} and D_{23} are the four-pole parameters between microphones 2 and 3. The specific expressions for the parameters are given in [19].
Figure 15 shows the set-up of the two-loads method. It leads to the same results of the two-sources process by changing the outlet impedance instead of the source location, so calculating the TL with Eq. 4 [18].

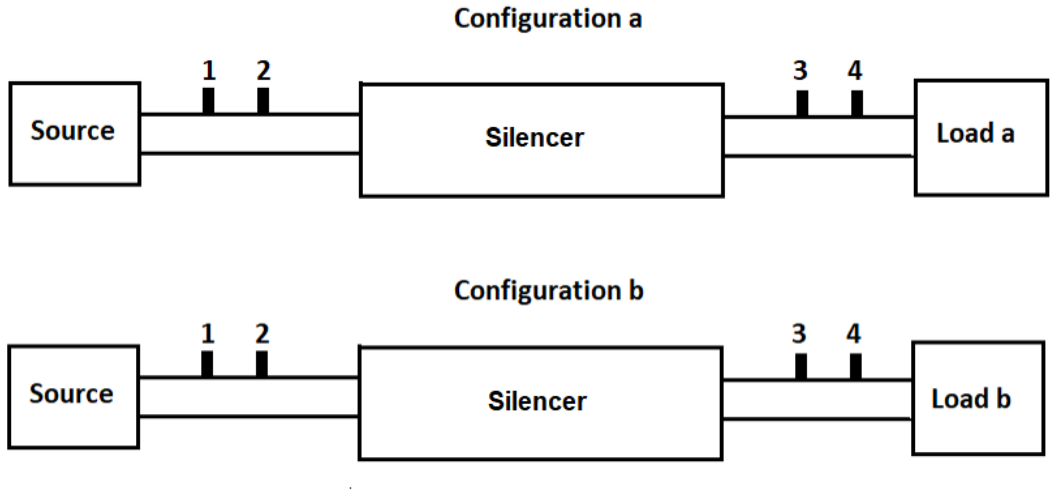

Figure 15. Measurement set-up according to the two-load method.

Different strategies allow for changing the termination impedance: two terminations with different lengths, terminations with and without absorbing material, or even a closed and an open-end. Of course, if the two loads are very similar, the results will be unstable.

Chapter 3

Numerical Modelling Strategies: Hint of Theory

Acoustic FEM and CFD are mostly used to evaluate the acoustic properties of a component. In the following sections, their modelling strategies along with their pros and cons are illustrated. Then, the proposed combined CFD-FEM approach is explained and compared with the few studies found in the literature that use a combined methodology.

1. Acoustic FEM

The finite element method is the most commonly used numerical prediction technique for solving engineering problems, which consists of finding the distribution of one or several field variables in a continuum domain, governed by an appropriate set of partial differential equations (PDEs) and boundary conditions. The finite element method is based on two concepts: the transformation of the original problem into an equivalent integral formulation, approximation of the field variable distributions and the geometry of the continuum domain in terms of a set of shape functions, which are locally defined within small subdomains (finite elements, Figure 16) of the continuum domain. Through the application of the element concept, the original problem of determining field variable distributions in a continuum domain is approximately transformed into a problem of determining the field variables at some discrete (nodal) positions within each element. This transformation results in a set of algebraic equations, for which numerical solution procedures are readily available [47].

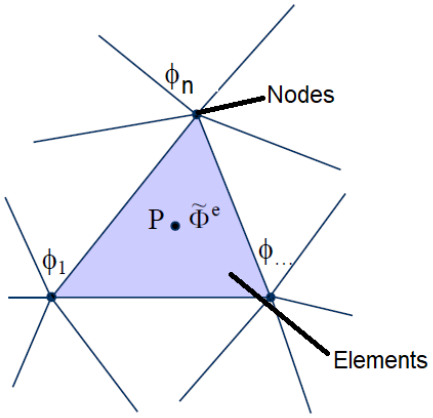

Figure 16: Generic element with nodes.

FEM approach is used to simulate acoustic problems for a long time, as those problems can be expressed by PDEs, for example, the Helmholtz equation that governs sound wave propagation in the air [48]:

$$\nabla^2 P_a + k_0^2 P_a = 0 \qquad \textbf{Eq. 5}$$

where P_a is the acoustic pressure, ∇ is the Laplacian operator and k_0 is the wave number in the air.

In this research the software Actran VI is used for FEM modelling of interior acoustic and TL evaluation. Actran VI use the decomposition technique (Chapter 2) to evaluate the TL, incident and reflected pressure waves at the inlet of the studied prototype and the transmitted pressure waves at the outlet are modelled using duct modes (Figure 17): the global pressure waves propagation in ducts results from a superposition of duct modes [42]:

$$P(f) = p^+ + p^- = \sum_{i=1,N} \alpha_i^+ \varphi_i^+ + \sum_{j=1,N} \alpha_j^- \varphi_j^- \qquad \textbf{Eq. 6}$$

were p^+ and p^- are the incident and reflected pressure wave, α is the modal amplitude and φ is the mode shape.

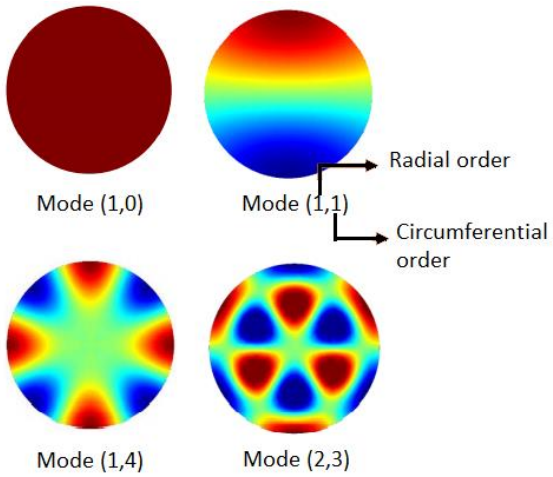

Figure 17. Example of acoustic mode shapes in circular ducts.

Note that, for a given duct section and a certain frequency, a limited number of modes propagate: each mode is defined by its cut-on frequency, the model is cut off below this frequency (evanescent mode) and is cut on above this frequency (propagating mode). Only the plane mode is always propagating.

The ISO standard [49] provides a frequency limit to ensure a plane wave propagation, without higher-order modes:

$$f < 0.586\ {}^{c}/_{D} \qquad \text{Eq. 7}$$

where D is the diameter of the largest pipe in the structure and c is the sound velocity in the medium.

The use of duct modes allows for analytically representing a semi-infinite duct (e.g., plane wave propagation with no reflection at the boundaries) that does not need to have meshed (Figure 18). This approach simulates the excitation at the inlet with imposed duct modes and the anechoic condition with free duct modes.

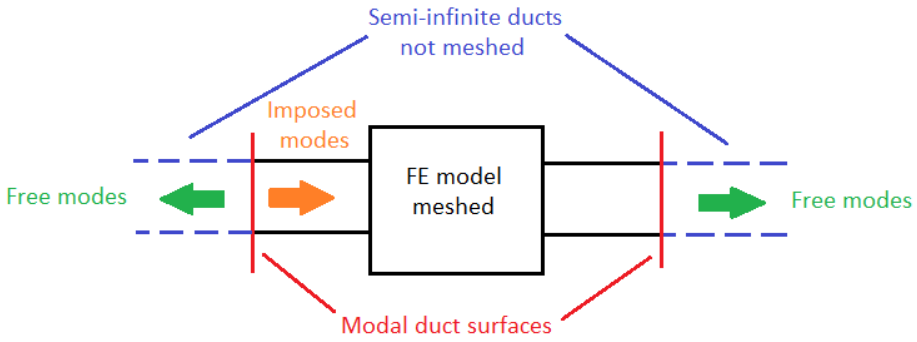

Figure 18. Schematization of the acoustic FEM model with duct modes.

The FEM approach, despite not properly considering the flow but only the fluid inside the component, represents an easy and fast method to estimate the TL of a component.

1.1. Modelling of Perforated Elements

Perforated elements, quite common in many acoustic systems, cause-specific dissipation when acoustic waves pass through the holes. Physical phenomena involved in a perforated plate can be split into two contributions: an inner contribution which represents the inner effects of the holes and the length correction term which represents the physical effects "outside" the holes. These two contributions have the same order of magnitude and should then be both taken into account in the perforated plate models.

Meshing such holes is cumbersome and lead to CPU-intensive models, so they are modelled inside the software environment considering an equivalent transfer admittance A derived from fluid characteristics and perforations geometry as follows:

$$A = {}^{1}/_{Z_p} \qquad \text{Eq. 8}$$

Z_p is the transfer impedance of the perforated element expressed as follows:

$$Z_p = {}^{Z}/_{\sigma} = {}^{1}/_{\sigma}\,(R_p + jX_p) \qquad \text{Eq. 9}$$

where Z is the transfer impedance for a single hole and σ is the porosity parameter that has a different expression depending on the type of hole distribution on the plate (e.g., triangular, squared, …). The *Rp* and *Xp* terms can be split into inner and length correction contributions in the following form:

$$R_p = R_p^{inn} + R_p^{corr}$$

$$X_p = X_p^{inn} + X_p^{corr} \qquad \text{Eq. 10}$$

The resistive part of the inner contribution R_p^{inn} corresponds to dissipation inside the viscous boundary layers of the perforation, whereas the reactive part X_p^{inn} represents the mass of fluid which participates tin the motion. The resistive end correction R_p^{corr} accounts for the frictional losses due to viscous effects at the surface of the plate, while the reactive end correction X_p^{corr} is due to the imaginary part of the radiation impedance at the tube's ends.

In Actran VI [50], the software employed in this study, the Maa formulation [51] is used to evaluate the transfer impedance, for fluid at rest while different strategies are available to consider the presence of both grazing [52,53] and bias flow [54]. To be able to use these formulations, the knowledge of at least the geometrical parameter of perforations and the material characteristics of the perforated elements are needed.

1.2. Modelling of Narrow Channel Components

Visco-thermal effects appear when sound waves travel through thin air layers or narrow channels and dissipation occurs due to the boundary layer created by viscosity.

Two different components can be used to model this kind of part in Actran VI: rigid porous component and visco-thermal component. Both components can take into account the mean flow effect (including temperature effect) and can model narrow channels without the need to drown and mesh the singles channels, but the mesh must be adapted

to ensure no "radial" propagation (e.g., plane wave) as acoustic waves propagate in independent narrow channels (Figure 19).

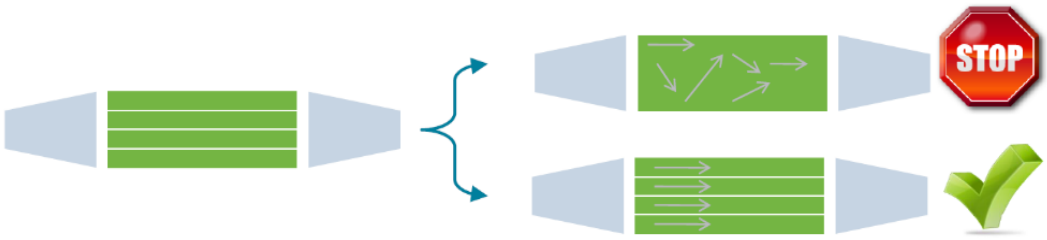

Figure 19: Example of allowed flow direction.

The rigid porous component is based on the Biot theory that treats and heterogeneous medium as an equivalent homogeneous medium [50,55], assuming the skeleton of the component is rigid. This approach needs the knowledge of fluid and skeleton properties, besides the fluid-skeleton interaction properties (Table 1), as a function of temperature and velocity if the presence of a mean flow is considered.

Table 1: Input data for rigid porous component in Actran VI.

Fluid	**Skeleton**	**Fluid-skeleton interaction**
Density	Density	Porosity
Bulk Modulus	Young Modulus	Flow Resistivity
Viscosity	Poisson Ratio	Biot Factor
Thermal Conductivity		Tortuosity
Specific Heats		

The bulk modulus measures the compressibility of the fluid within the pores, for pores filled with air is 140000 N/m^2 in adiabatic conditions and 101325 N/m^2 in isothermal conditions. The Biot factor can be assumed equal to 1 for most materials. The tortuosity coefficient measures the complexity of the path an air particle must follow to proceed from one point to another point, for straight channel its value is 1. The porosity is defined as:

$$\Omega = {V_f}/{V_t} \qquad \textbf{Eq. 11}$$

where V_f is the volume of fluid contained in the total volume V_t of the porous material.
The flow resistivity is a measure of the resistance that a fluid flowing through a porous material encounters and it is related to the viscous interaction forces between the fluid and the solid skeleton. Its expression can be derived from the Hagen–Poiseuille equation [56] that gives the pressure drop in a fluid flowing through a long cylindrical pipe:

$$\Delta \boldsymbol{P} = {\boldsymbol{8\mu h \cdot v}}/{\boldsymbol{r^2}} \qquad \textbf{Eq. 12}$$

where ΔP is the pressure drop, h is the length of pipe, μ is the dynamic viscosity, r is the radius and v is the velocity of the flow. The above equation can be applied to each cylindrical pipe of a component composed of narrow channels (e.g., catalyst). Moreover, in a porous material, the resistivity can be related to the pressure drop as follow:

$$\boldsymbol{R} = {\boldsymbol{\Omega \cdot \Delta P}}/{\boldsymbol{hv}} \qquad \textbf{Eq. 13}$$

Combining Eq. 12 and 13 the following expression can be derived for the flow resistivity in cylindrical narrow channel component:

$$\boldsymbol{R} = {\boldsymbol{8\mu\Omega}}/{\boldsymbol{r^2}} \qquad \textbf{Eq. 14}$$

where r is the radius of a channel.
The visco-thermal component requires to know fewer properties: fluid characteristics, the porosity of the component and the channel shape (e.g., radius for cylindrical channel).
This approach involves the reductions of the full Linearized Navier-Stokes-Fourier equations into an equivalent fluid scalar equation involving only the acoustic pressure (also called equivalent fluid equations). Actran implements the low reduced frequency (LRF) model developed by Beltman [57] with the extension proposed by Sambuc et al. [58] which handles the presence of a mean incompressible flow inside the fluid domain within waveguide geometries (e.g., thin layer and narrow channel).
The LRF model implies the hypothesis of plane wave propagation through the waveguide and is valid for a particular range of dimensionless shear wavenumber (Eq.15) and reduced frequency $\overline{k_0}$ (Eq.16) as illustrated in Figure 20. This figure also shows the domain of validity of conventional wave models which do not incorporate viscous effects.

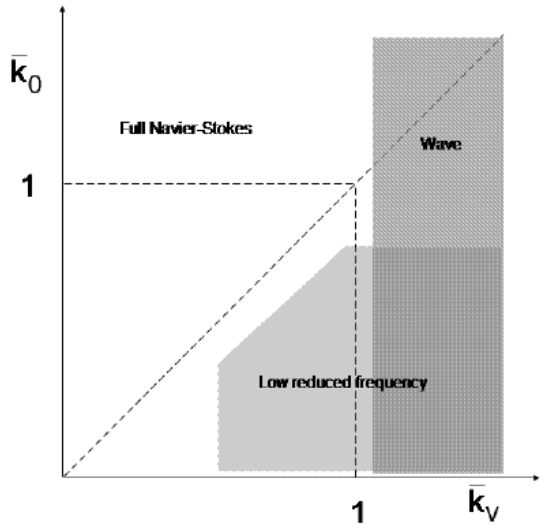

Figure 20: Validity of LRF model.

$$\overline{k_0} = lk_0 = l\,\omega/c_0 \qquad \textbf{Eq. 15}$$

$$\overline{k_v} = lk_v = l\sqrt{\rho_0\omega/\mu} \qquad \textbf{Eq. 16}$$

The dimensionless shear wavenumber $\overline{k_v}$, where l is a length scale (thickness of a thin layer or radius of a narrow tube), ω the angular frequency and ρ the fluid density, is measure of the ratio between inertial effects and viscous effects in the considered gas. For large $\overline{k_v}$ values, the inertial effects dominate while viscous effects are dominant for low $\overline{k_v}$ values.

The final equivalent fluid model is obtained from the continuity equation of LNSF by substitution of the equation of state, the thermal and the shear velocity solutions. The pressure wave equation is integrated over the cross-section and leads to the following 1D dissipative convective wave equation [50]:

$$\nabla_{pd}\left(H\nabla_{pd}p'\right) - \widehat{M_0^2}\gamma N^{-1}\nabla_{pd}^2 p' - 2ik_0\gamma N^{-1}\widehat{M_0}\nabla_{pd}p' + k_0^2\gamma N^{-1}p' = ik_0R \qquad \textbf{Eq. 17}$$

where $\widehat{M_0}$ is the mean Mach number, R the source term derived from the velocity along the cross-sectional direction, γ the ratio of specific heats, ∇_{pd} the gradient along the propagation direction and p' the acoustic perturbation of pressure.

This wave equation is a generalization of the conventional convective Helmholtz equation which introduces thermo-viscous dissipation through the complex parameters H and N (dimensionless factors corresponding to corrective terms for the density and the bulk modulus respectively). It is also a generalization of the LRF equation given by Beltman considering the effect of a mean flow.

2. CFD

Viscous fluids are described by three PDEs which represent the conservation of mass (the continuity equation), momentum (equation of moment) and energy, which are the so-called Navier-Stokes equations. These equations can be solved analytically only in simple cases (e.g., laminar flows), so the Reynolds Averaged Navier Stokes equations (RANSE) are usually used to describe the motions of fluids.

The CFD approach can be based on the finite volume method, which makes use of the integral form of RANSE. The domain is divided into adjacent control volumes (Figure 21) and conservation equations are applied to each volume (usually at the center), leading to a system of algebraic equations that can be numerically solved. Interpolation is then used to evaluate the variable values on the faces of the control volume, approximating both surface integral (e.g., fluxes) and volume integral (e.g., volume forces) [59].

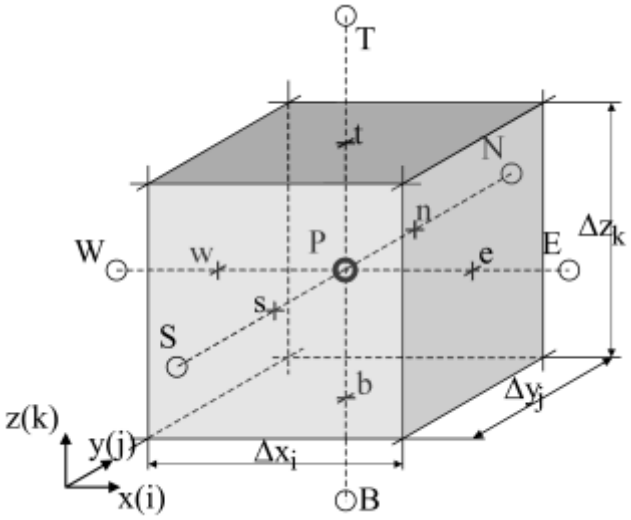

Figure 21: Example of the control volume.

In this research, Star-CCM+ is used to perform CFD simulations. To evaluate the TL of a component, three steps are needed: a first steady-state simulation computed to have a steady flow used as the initial condition for two subsequent unsteady-state simulations,

one with a constant mass-flow and one with an acoustic excitation superimposed to the constant mass-flow.

In this study a half-sinusoid wave impulse with suitable amplitude is used as acoustic excitation; it is capable to provide a rather flat frequency spectrum for the wave incident on the studied component. The TL is calculated using the decomposition technique (Chapter 2), so three control points are set in the computational domain, as depicted in Figure 13, where pressure and velocity signals are registered during the unsteady simulations. The distances between microphones have to be chosen by guidelines [49] based on the studied frequencies. Also, the position of the measuring point concerning the inlet/outlet of the component or any variation in diameter or direction of the pipes has to be carefully evaluated to achieve a flow as homogeneous as possible [60]. Moreover, a Non-Reflecting Boundary Condition (NRBC) is set on both the inlet and the outlet to avoid reflections and reach the anechoic conditions.

The acoustic signals are then determined by the difference between the signals of the two unsteady computations. The sound pressure signals in the time-domain are converted into the frequency domain by an FFT with prescribed parameters [61].

In preparing the CFD model, particular attention has to be paid to the base size (*bs*) of the mesh that should satisfy the following relation, based on the maximum analyzed frequency (f_{max}) and the speed of sound in the medium:

$$bs = {}^{c}/_{4f_{max}} \qquad \textbf{Eq. 18}$$

Of course, also the flow conditions have to be taken into account, for example setting refinement areas to capture complex phenomena when the flow passes through perforations.

For unsteady computations, the time-step has to be set to guarantee a sufficient number of sampling points in the period of a signal with a prescribed frequency to not have aliasing during the passage from the time domain to the frequency domain.

CFD approach allows considering the influence of flow conditions on the acoustic attenuation of components. However, the CFD simulations may represent a limit for the computational costs and complexity, especially in the earlier stage of the design process, where the flow conditions may be unknown making difficult the settings of the simulation.

2.1 Modelling of Perforated Elements and Narrow Channel Component

Two strategies are available in Star-CCM+ to model perforated elements and narrow channel components, that allow avoiding drawing and meshing the single holes and channels.

The cross-flow through perforated elements can be modelled using a porous baffle interface, while the flow flowing through a narrow channel can be modelled using a porous region. Both these methods are based on the Darcy-Forchheimer law, reported in the following equation:

$$\Delta P/L = -(\nu\alpha + 1/2\, V\beta)V \qquad \text{Eq. 19}$$

where ΔP is the pressure drop, L is the length of the porous media, ν is the kinematic viscosity, V is the fluid velocity and α and β are the viscous and inertial resistance coefficients, respectively. This equation describes the flow through a porous media [62]. In order to restrict the flow in the directions perpendicular to the primary direction in the porous region, a resistance coefficient that is 2-3 orders of magnitude larger than the primary coefficient has to be chosen.

Our preliminary study [29], which is part of this thesis (Appendix 2), showed that the use of a porous baffle interface is not suitable for modelling perforated elements in terms of both computational burden and accuracy of results. Accordingly, the perforations are modelled using the real geometry in the following parts. Indeed, the use of porous region is useful to model the flow through narrow channel components, such as catalytic converters or tower packing, even if the input parameters (i.e., porosity, tortuosity and flow resistance coefficients) are properly set.

3. Combined CFD-FEM Approach

The combined approach aims to exploit the advantages of CFD and FEM approaches to obtain an efficient and accurate model to evaluate the acoustic properties of exhaust line components.

Two fundamental advantages derive from the use of this methodology. First of all, the acoustic properties, such as TL, of a component can be easily calculated with the acoustic FEM model, provided that a reliable flow field is calculated with the CFD model The

FEM model can calculate just an approximation of the flow field, especially for in-pipe fluxes, as it uses the approximation of potential flow. In a recent paper [63] it shown that unsteady CFD simulations are not needed to properly evaluate the TL of a component in presence of flow; a steady which computes the flow field is sufficient to reach reliable results, with a benefit in terms of computational effort.

The second advantage is represented by the possibility to evaluate the noise generated by the flow without the need for CFD unsteady simulation. The Stochastic Noise Generation and Radiation (SNGR) [64] method allow for building unsteady turbulence from mean flow parameters (e.g., turbulent kinetic energy, dissipation and mean velocity field) extracted from a steady CFD simulation. So, the source generation process for the study of noise-induced by the flow is based on two steps: derivation of turbulent velocity from parameters extracted from the CFD, source computation using Lighthill [65] and Möhring [66] analogies.

In Figure 22 the workflow of the combined approach is reported.

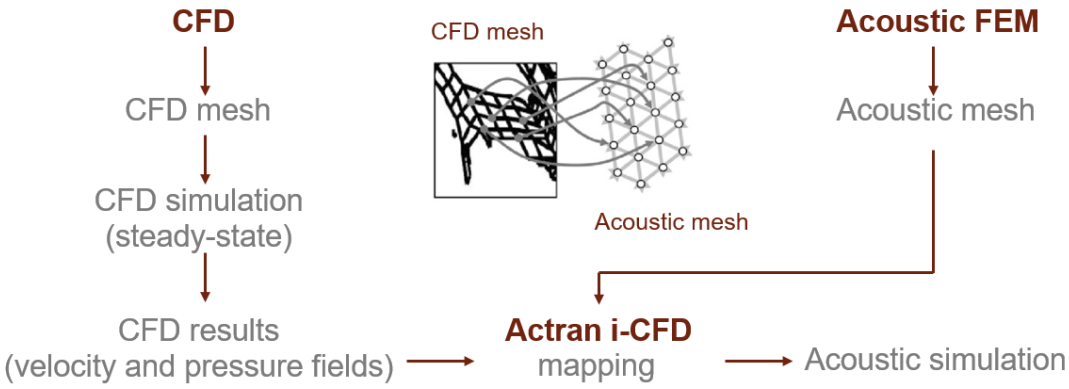

Figure 22: Workflow of combined CFD-FEM approach.

Actran i-CFD is a tool that allows performing mesh mapping of the flow field and related properties from CFD mesh to acoustic FEM mesh. This procedure involves two steps: first of all, the nodes of the CFD mesh have to be projected on the acoustic mesh (Figure 23); then the projected values are interpolated and mapped on the FEM mesh nodes based on the shape functions. Note that, to avoid loss of information, the CFD mesh has to be finer than the FEM one.

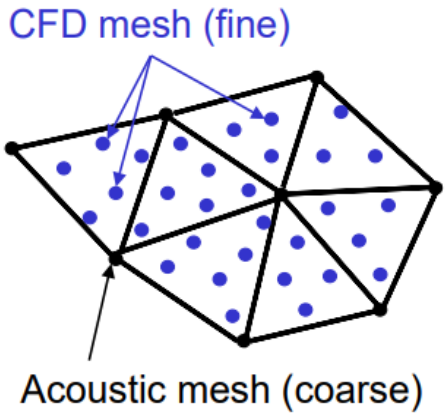

Figure 23: Mapping from CFD to acoustic mesh.

Chapter 4

Application of the Combined CFD-FEM Methodology: Results and Discussion

The acoustic properties of marine exhaust line component were investigated as a function of the flow parameters (e.g., temperature and velocity) and the viscous dissipations.

The flow field is calculated with CFD simulations and then, the average values of the flow parameters are imported into the FEM solver to estimate the TL. The calculated fields are transferred from the CFD mesh to the FEM one through mesh mapping (see Chapter 3, Section 3).

As above reported, for the combined approach, the CFD model does not require the same complexity and detail level of a full CFD computation, neglecting the impulse excitation, the NRBC and the control points.

To carry out this research, in the first instance, the validity of our CFD-FEM methodology is assessed on simplified geometries such as a straight-tube perforated silencer (Appendix 5, Figure A5-I) and a model-scale scrubber with perforated plate (Appendix 3, Figure A3-V).

The numerical model is then used to evaluate the TL of a real system and specifically the DOC (Appendix 4, Figure A4-VI) mounted on the exhaust line of the diesel Genset mockup (Appendix 6, Figure A6-I). The acoustic properties of the DOC are optimized through a numerical optimization process and finally the combined methodology is used to evaluate the TL of the optimized DOC in series with an ad hoc designed scrubber (Appendix 4, Figure A4-VII).

The CFD-FEM approach allow to evaluate the values of the back pressure generate by each component, besides the acoustic properties. This value must not exceed prescribed limits to avoid negative influence the engine efficiency. Accordingly, this is an important piece of information for a device design.

The CFD model accuracy is evaluated against literature data (Appendix 5), while FEM model accuracy is evaluated against experimental measurements (Appendix 4).

Chapter 4

1. Straight-Tube Perforated Silencer

The flow fields for the straight-tube perforated silencer described in Appendix 5, Figure A5-I, is calculated with both steady and unsteady-state CFD simulations, in order to compare the TLs obtained importing in the FEM solver the steady flow or the mean flow calculated from the unsteady simulation.

The mesh and the physical models are set as in Appendix 5 for both the steady and the unsteady-state simulations. The boundary conditions are set as in the preliminary study (Appendix 5) but without the NRBC. Table 2 summarizes the geometrical parameters and boundary conditions employed in the experiment.

Table 2: Summarizing geometrical parameter and boundary conditions of straight-tube perforated silencer.

D inlet/outlet [mm]	**D chamber [mm]**	**L inlet/outlet [mm]**	**L chamber [mm]**	**d perforations [mm]**	**Porosity [%]**	**Tickness [mm]**
32	110	125	200	6	9	2
Mass-flow inlet [kg/m2]	**Pressure outlet [Pa]**	**Temperatures [K]**				
41	101325	288				

In these simulations there is no need to set control points, unless the evaluation of the pressure drop is needed (one control point needed in the inlet pipe).

The flow fields obtained with both the steady and unsteady simulations are reported in Figure 24.

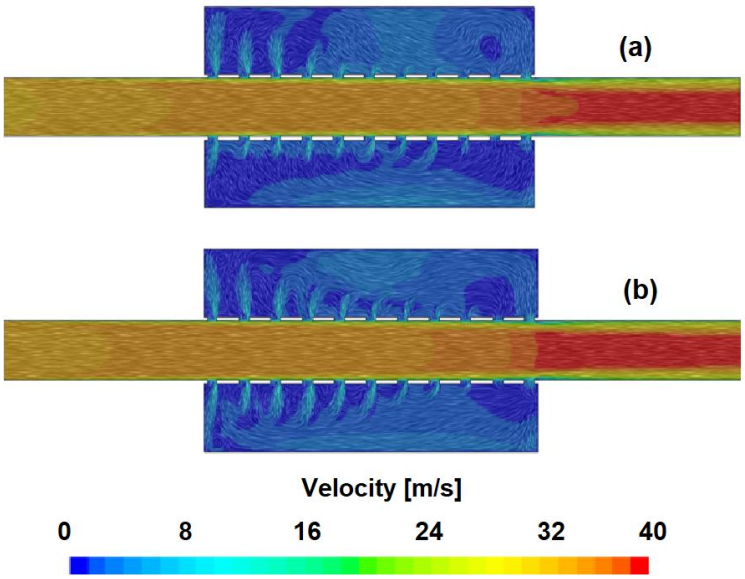

Figure 24: Flow velocity with (a) steady simulations and (b) unsteady simulation. Inlet on the left side and outlet on the right side.

The flow fields are imported through mesh mapping from the CFD mesh to the FEM one (Figure 25). In the FEM model the holes are not drawn and meshed as they are modelled using transfer admittance (Section 1.1 of Chapter 3).

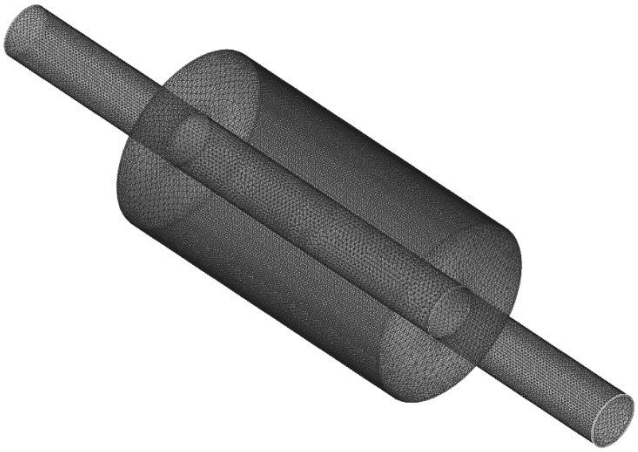

Figure 25: FEM mesh for straight-tube perforated muffler.

With the same settings and methodology explained in Section 1 of Chapter 3, the TLs of the straight-tube perforated silencer is then calculated with the FEM software considering both the steady flow and the mean flow calculated from the unsteady simulations.
The calculated TLs are reported in Figure 26 and compared with both literature CFD and experimental literature data, as well as with TL calculated with FEM not considering the

flow. TL curves obtained with both the flow fields extracted from the steady and the unsteady-state CFD simulation are nearly coincident. This clearly suggests that the unsteady CFD simulations are not strictly necessary to describe the problem, which makes the combined approach faster and easier to implement, since only steady CFD simulation is needed to calculate the flow field. This is in accordance with literature [67] that highlight that for flow with a velocity ≤ 0.3 Ma the greatest influencing parameter on the TL is the temperature, especially at the low-medium frequency. Thus in following computations only steady CFD simulations are used in the combined approach.

In Table 3 the CPU (Central Processor Unit) time employed for the combined approach is compared with those required for the two unsteady CFD simulations to the times required for the two unsteady simulations of the CFD approach (characteristics of used hardware are reported in Appendix 1): the proposed methodology takes 1% of the time needed for the CFD approach.

Moreover, considering the TL obtained with the FEM model and the CFD-FEM approach, it is possible to highlight the influence of the flow that lead to a damping of the sharp peak around 3000 Hz (Figure 26).

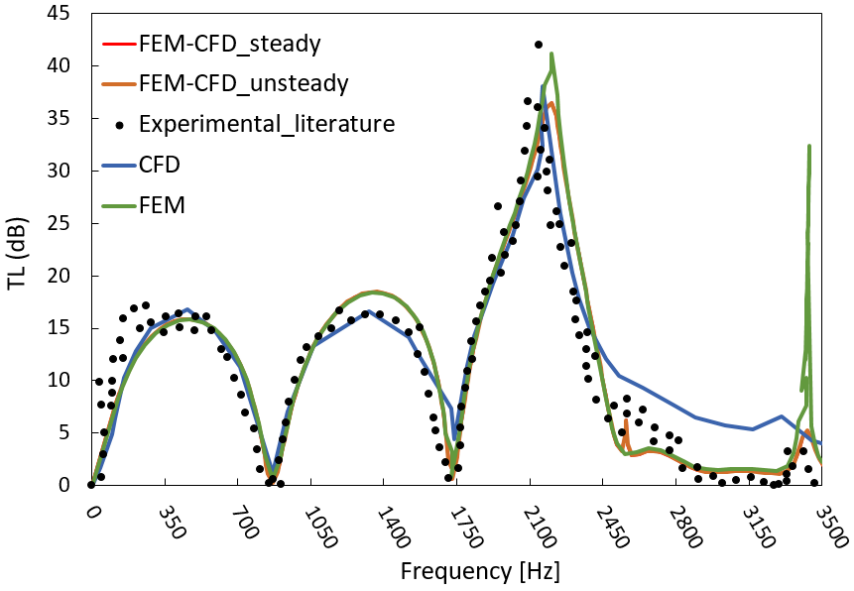

Figure 26: Comparison between TL of straight-tube perforate silencer calculated with FEM and CFD-FEM approach and literature CFD/experimental data.

Table 3: Comparison between CPU time of different numerical approaches.

	CFD-FEM approach	CFD unsteady	CFD impulse
CPU Time [s]	25×10^4	15×10^6	15×10^6

2. Model-Scale Scrubber with Perforated Plate

The combined approach is used to estimate the influence of both the flow velocity and temperature on the TL of the model-scale scrubber with perforated plates (Appendix 3). In Table 4 the geometrical parameter and boundary conditions are summarized.

Table 4: Summarizing geometrical parameter and boundary conditions of model-scale scrubber with perforated plates

D inlet/outlet [mm]	D chamber [mm]	L inlet/outlet [mm]	L chamber [mm]	H inlet [mm]	H conical adapter [mm]
35	85	100	1010	150	50
Distance between plates [mm]	**H first plate [mm]**	**d perforations [mm]**	**holes spacing [mm]**	**Tickness [mm]**	
250	325	6	9	1	
Velocity inlet [Ma]	**Pressure outlet [Pa]**	**Temperatures [K]**			
0.1-0.2	101325	300-473			

Both the CFD and FEM meshes are created following the study and the guidelines reported in Appendixes and in Chapter 3. The settings are set in accordance with the proposed methodology previous explained. The perforated plates are modelled considering the real geometry (Appendix 3, Figure A3-V).

Figure 27 shows the comparison between the obtained TL: the sharp peak around 1700 Hz is dampened as both the flow velocity and temperature increase while at lower frequency the TL remain constant for this geometry.

A very important result of this investigation, in view of a device design, is the flow velocity field as calculated from CFD (Figure 28): at the inlet of the model scale-scrubber; the incoming flow collides with the opposite wall of the scrubber, which generates vorticity resulting a non-homogeneous flow on the first plate, suggesting poor “chemical

performance" of such a design. For this reason, in the subsequent scrubber prototype with tower packing, the inlet pipe is connected with a rotatable joint in order to orient the inlet flow to generate a flow field as homogeneous as possible at the inlet on the packing, thus optimizing both the chemical abatement efficiency and noise reduction.

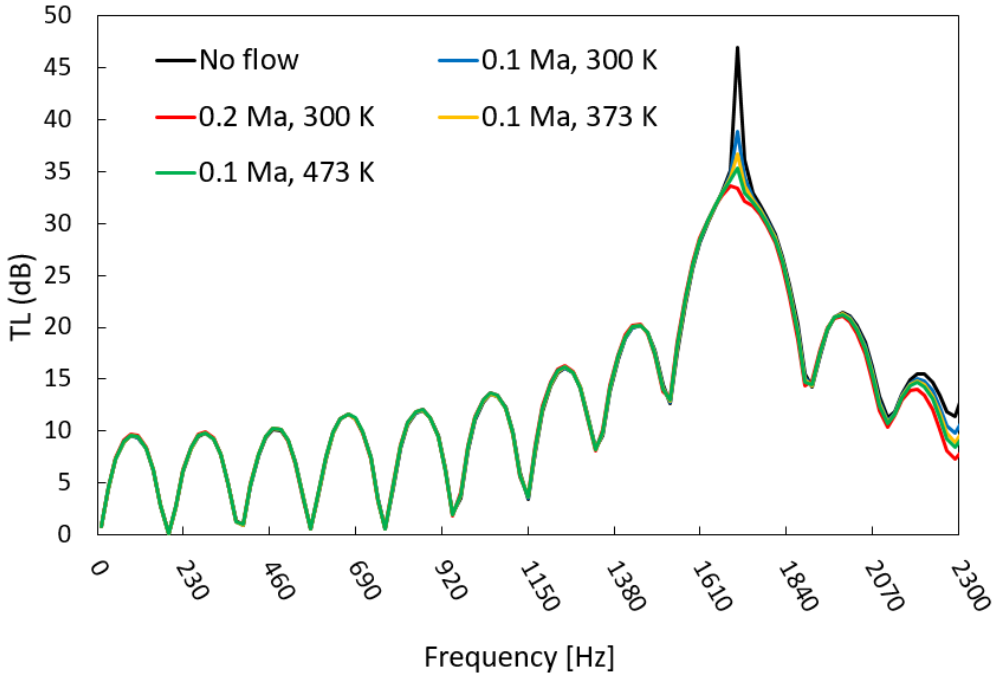

Figure 27: TL at different flow velocities and temperatures.

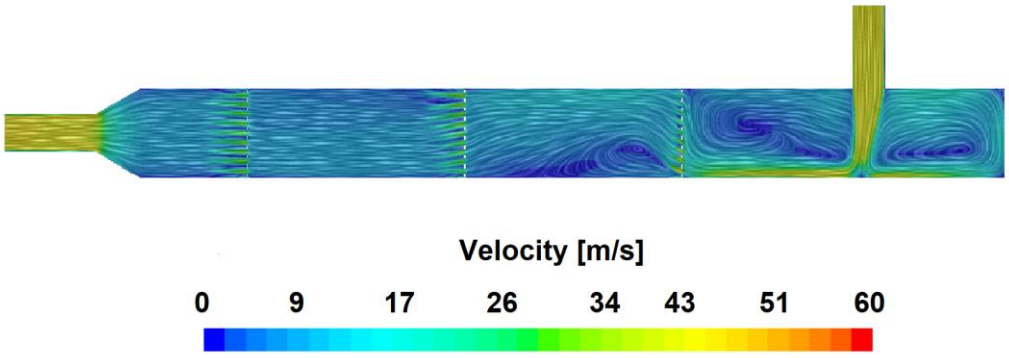

Figure 28: Velocity flow field at 0.1 Ma.

3. DOC

The combined approach, with settings as previously explained, is used to evaluate the TL of the DOC (Figure A3-VI) mounted on the exhaust line of the Genset (Appendix 6,

Figure A6-I). The CFD mesh (Figure 29) is created on the basis of the studies reported in the Appendixes.

Velocity and temperature (44 m/s and 270 °C respectively) are set in accordance with experimental measurements (Table A6-IV) at the inlet, considering the open-end configuration. In Table 5 the geometrical parameter and boundary conditions are summarized.

Table 5: Summarizing geometrical parameters and boundary conditions of DOC

D inlet/outlet [mm]	**D chamber [mm]**	**L inlet/outlet [mm]**	**L chamber [mm]**	**L conical adapters [mm]**
88.9	296	100	510	125
L catalysts [mm]	**Distance between catalysts [mm]**	**R [N·s/m3]**	**OAR [-]**	
90	60	678	0.92	
Velocity inlet [m/s]	**Pressure outlet [Pa]**	**Temperatures [K]**		
44	101325	543		

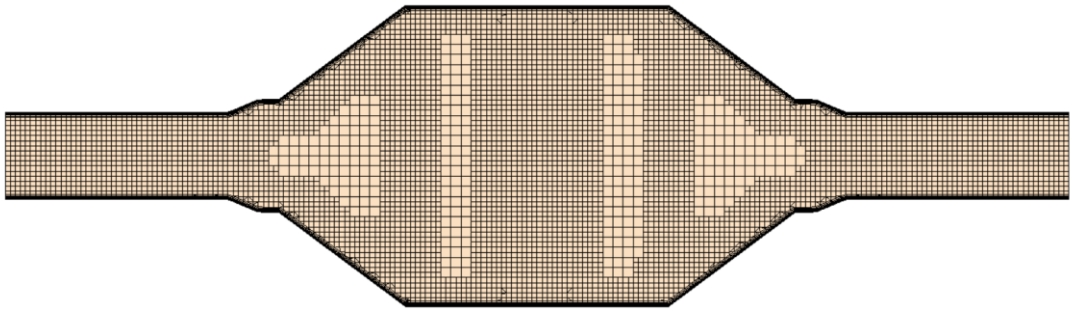

Figure 29: CFD mesh employed for DOC discretization.

The catalysts inside the DOC (Appendix 3) are modelled using porous region, but instead of using the procedure proposed by Star-CCM+ to calculate resistance coefficient (Chapter3, Section 2.1) the following method is applied.

In a straight pipe, pressure drop is caused by energy loss due to frictional forces between the flowing medium and the pipe walls and can be expressed as follow [68]:

$$\Delta P_{friction} = \varepsilon \, {}^{L}/_{D} \, {}^{1}/_{2} \, \rho u^{2} \qquad \textbf{Eq. 20}$$

where ε is the Darcy friction factor, L the pipe length, D the pipe diameter, ρ the fluid density and u the mean flow speed.

The Darcy friction factor value can be derived from the Moody diagram as a function of Reynolds number (Re) and pipe roughness [68]. For laminar flow, as assumed in the narrow channel of the catalysts, ε can be expressed as follow:

$$\varepsilon = {}^{64}/_{Re} \qquad \textbf{Eq. 21}$$

Combining Eq. 21 and Eq. 20 the Hagen-Poiseuille equation (Eq. 12) is obtained, thus the flow resistivity can be expressed with Eq. 14, using the hydraulic radius of the sinusoidal shape of the catalysts channels. The hydraulic radius is expressed as follow:

$$r_h = 4d_h = {}^{A}/_{p} \qquad \textbf{Eq. 22}$$

where A is the cross-sectional area of the channel and p the wet perimeter.

The catalyst used in this study has an Open Area Ratio (OAR) of 0.92 and a hydraulic diameter of a channel equal to $0.62 \cdot 10^{-3}$ m, leading to a flow resistivity of 678 $N \cdot s/m^4$ at 270 °C (exhaust gas temperature).

Figure 30 and Figure 31 report respectively the velocity and the pressure fields obtained from the steady CFD simulation, while Table 6 reports the temperature, velocity and relative pressure values calculated in the same location of the probe during experimental measurements (Appendix 6). The ΔP between DOC inlet and outlet and the generated back pressure are derived (Table 6) and compared with those experimentally measured with a Pitot tube (Table 6A-IV); Table 7 reports the differences in both Pa and percentage. Considering, besides the numerical error, the error of the experimental measurement caused by both the sensitivity of the instrumentation used and the difficulties of the measure itself (e.g., difficulty in positioning the probe due to the high temperatures of the pipeline, disturbed flow due to elbows and joints, …), a maximum discrepancy between numerical and experimental data of 15 % it is consider a good fitting results. Importantly, this measurement/calculation allows to verify that the back pressure generated by the DOC does not overcome the maximum allowable back pressure of the Genset that is 4900 Pa.

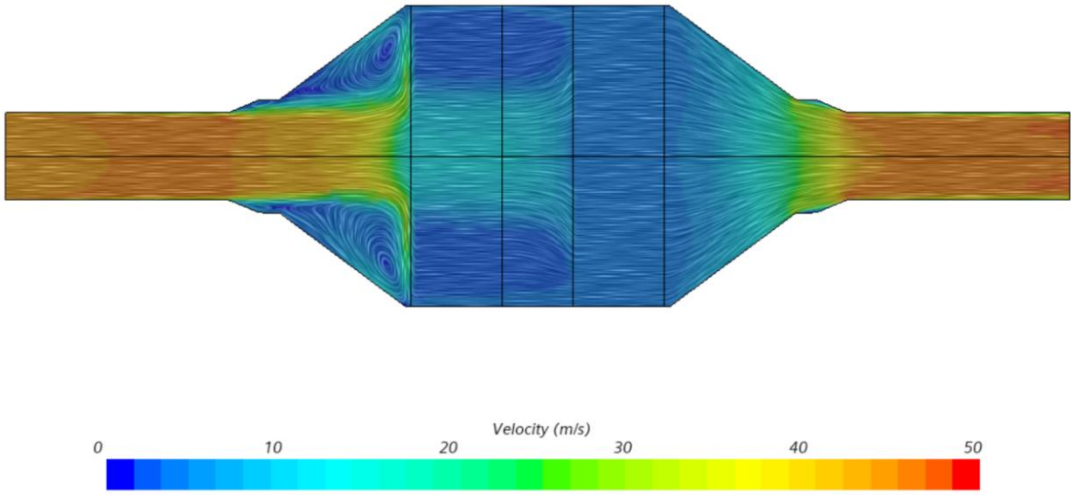

Figure 30: Velocity flow field. Inlet on left side and outlet on right side.

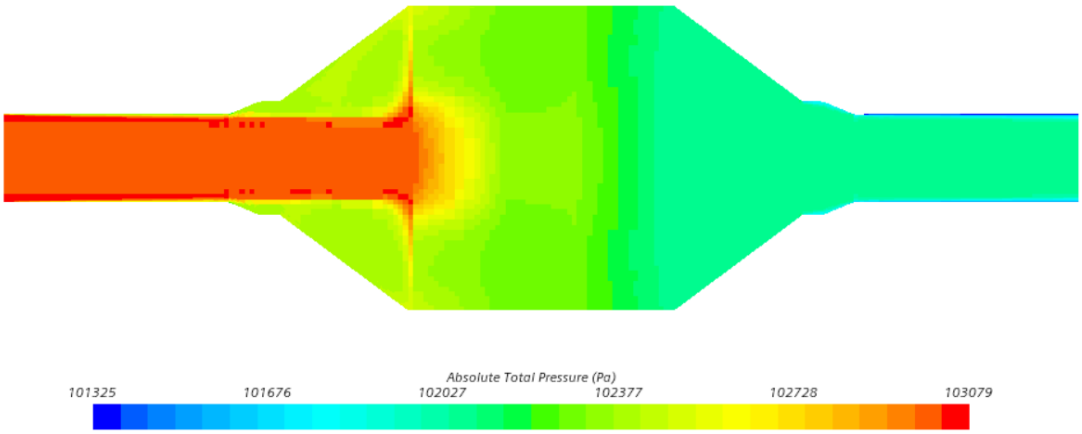

Figure 31: Absolute total pressure flow field. Inlet on left side and outlet on right side.

Table 6: Numerical values obtained at the inlet and at the outlet of the modelled DOC.

	Temperature [°C]	**Velocity [m/s]**	**Relative Pressure [Pa]**	**ΔP [Pa]**	**Back Pressure [Pa]**
In	269.9	45.6	1458	628	1458
Out	269.9	43.9	830		

Table 7: Comparison between numerical and experimental pressures.

	ΔP difference	Back Pressure difference
[Pa]	68	188
%	12	15

In order to numerically evaluate the TL of the DOC, the flow field calculated with the CFD is transferred on the FEM mesh (Figure 32) through mesh mapping. In Figure 33 the velocity field imported in the acoustic FEM is reported.

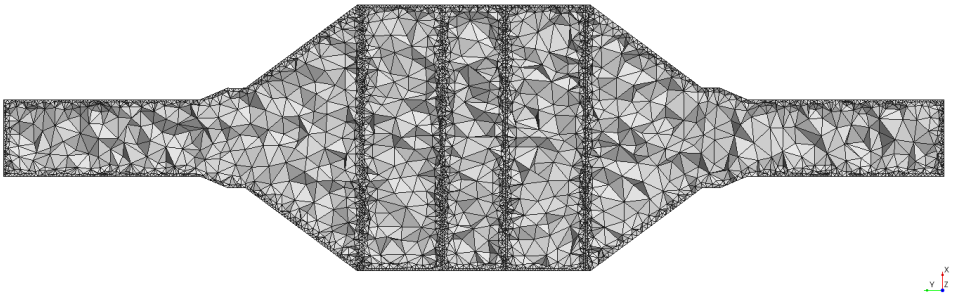

Figure 32: FEM mesh.

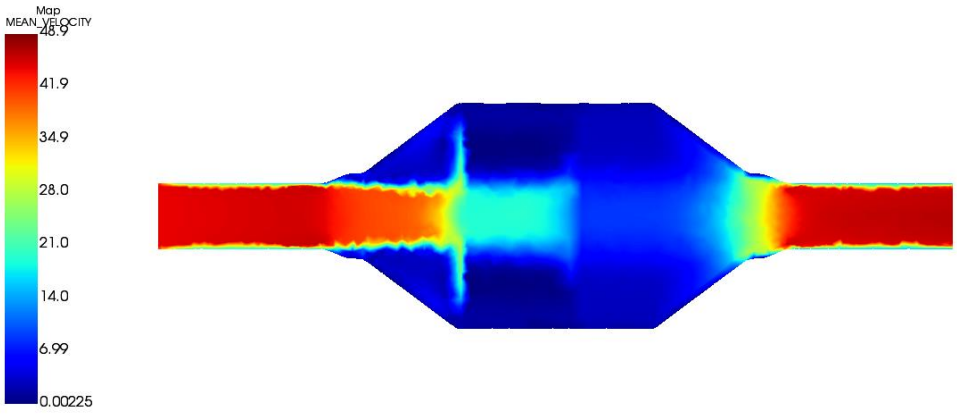

Figure 33: Velocity flow field imported in the FEM model.

The FEM model is set-up as explained in Chapter 3 and the catalysts are modelled using visco-thermal component as it better fit experimental data (Appendix 4). In Figure 34 the obtained TL is reported and compared with the TL calculate without the flow. The presence of the flow (i.e., temperature and velocity) tends to shift the TL curves towards higher frequencies.

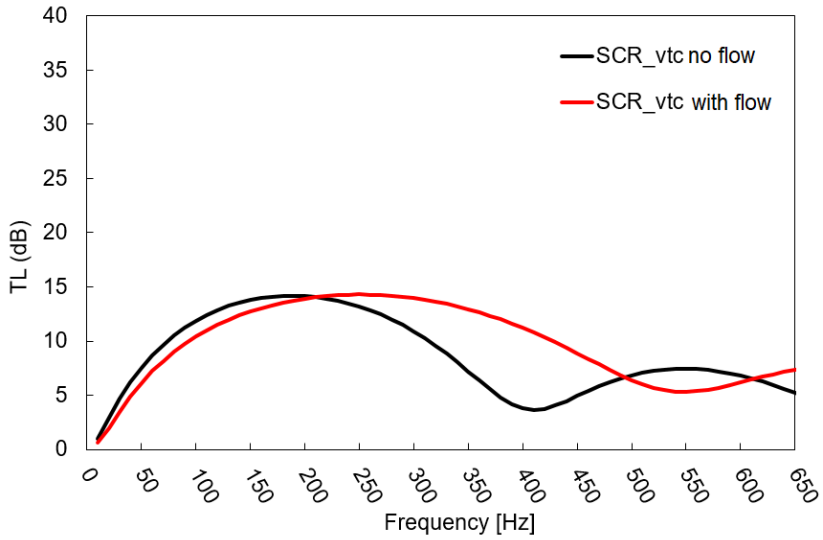

Figure 34: Comparison of TL with and without flow.

4. Optimization of Acoustic Performances of DOC

In this study the Response Surface Methodology (RSM) is used to optimize the TL of the DOC. The RSM involves the following fundamental steps: design a series of experiments for adequate and reliable measurement of the analyzed response, creation of a mathematical model that fit the real-valued response, analysis of optimum operating conditions.

Design of Experiment (DoE) can be used to create the database of TL values as a function of predetermined parameters needed to construct the metamodel. The predictor parameters with their constraints constitute the design space.

In the presented study, the following characteristics have been selected as predictor variables: length of the DOC (L), angle of the conical expansion (Θ), length of the catalysts (l), length of the interstice between the catalysts (i), DOC diameter (D), length of perforated pipe at inlet/outlet (lf), the adding of perforated plates (np), perforations diameter (Df), flow resistivity of the catalysts (R), OAR of catalysts. Figures 35 and 36

show the geometrical variable set on a notional scrubber geometry. In Table 8 the upper and lower limits for each variable are reported, these limits are established basing on chemical considerations and constraint. As a matter of fact, to ensure an efficient NO_x abatement a series of parameters has to be controlled and respected, for example the contact time between exhaust gas and catalysts or adequate cell dimensions so that they do not become clogged due to particulate matter [12]. The adoption of simple fractional design methods or derived ones (e.g. central composite designs or Box-Behnken methods) for the DoE determination of the simulation scenario is not advisable due to the complexity of possible mutual interactions of design parameters on predicted TL values. To this end, an alternative strategy has been used for the TL database creation, i.e. the adoption of a Stratified Latin Hypercube Algorithm. The representation of the resulting design space is reported in Figure 37.

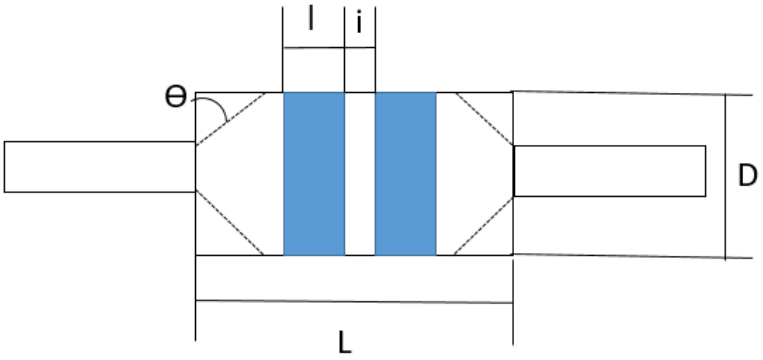

Figure 35: DOC dimensions used as predictor variables.

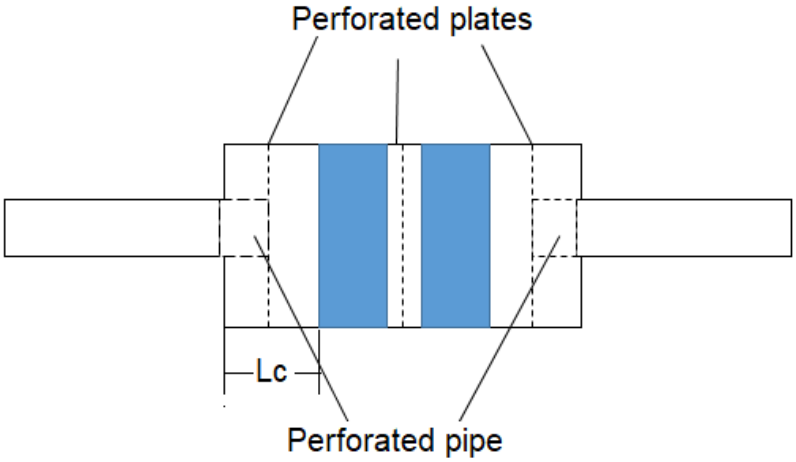

Figure 36: Elements added to the standard alternatively.

Table 8: Predictor variables and their limits.

	D [mm]	Θ [deg]	L [mm]	l [mm]	i [mm]	Df [mm]	R [N·s/m^3]	OAR [-]	Lf [mm]	np [-]
max	598	45	1020	180	120	35	678	0.98	Lc/2	3
min	297	0	510	90	60	10	520	0.92	0	0

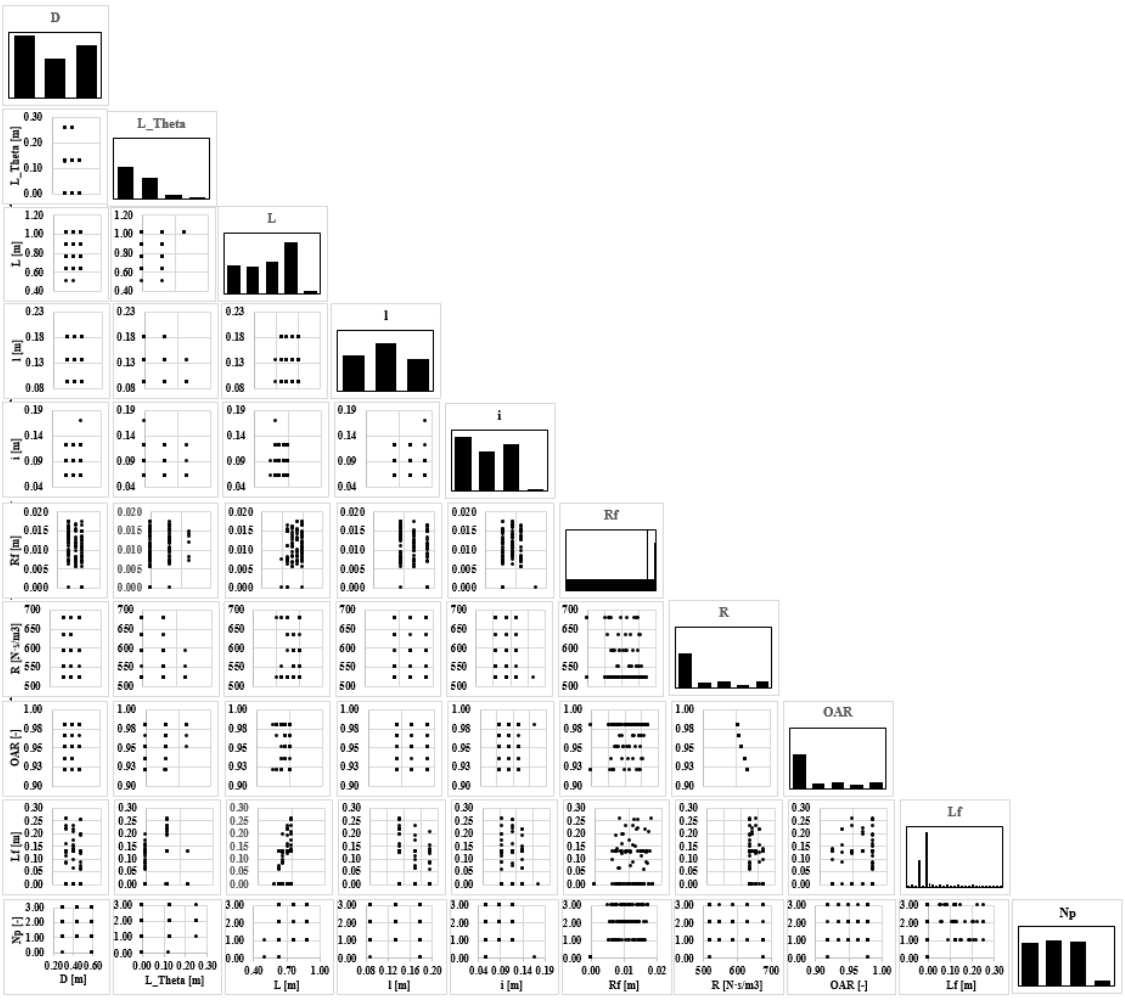

Figure 37: Construction of design space.

Once a TL database is generated employing multiple calculations with the proposed combined FEM-CFD numerical methodology for each case found through DOE, a multiple linear regression is used as mathematical surrogate model for TL prediction. The multiple linear regression can be expressed in vectorial form as follows [69]:

$$\boldsymbol{y = bX + e} \qquad \textbf{Eq. 23}$$

where *y* is the vector of measured values (TL in this case), *X* is the matrix of predictor variables, *b* is the vector of coefficient estimated by the regression and *e* in the error vector.

In this study, regressions are performed using a stepwise selection process [70]. Regressions on TL values pertain to specific frequencies from 50 to 400 Hz, more precisely in steps of 50 Hz. The stepwise process automatically selects the predictor variables significant to the model. The quality of the obtained regressions is assessed by means of the determination of coefficients R^2 and $R^2_{adjusted}$ (Table 9) defined as follows [69]:

$$\boldsymbol{R^2 = 1 - {SSE}/{SST}} \qquad \textbf{Eq. 24}$$

$$\boldsymbol{R^2_{adjusted} = 1 - \left({SSE}/{dfe}\right) \Big/ \left({SST}/{dft}\right)} \qquad \textbf{Eq. 25}$$

where *SSE* and *SST* are respectively the sum of squares errors and the sum of squares total, while *dfe* and *dft* are the corresponding degrees of freedom.

$$\boldsymbol{SSE = \sum_i^n (y_i - \hat{y}_i)^2} \qquad \textbf{Eq. 26}$$

$$\boldsymbol{SST = \sum_i^n (y_i - \bar{y})^2} \qquad \textbf{Eq. 27}$$

$$\boldsymbol{dfe = n - p - 1} \qquad \textbf{Eq. 28}$$

$$\boldsymbol{dft = n - 1} \qquad \textbf{Eq. 29}$$

where *n* is the number of real-valued responses to fit, *p* is the number of predictors included in the regression, y_i the real-valued responses to fit, $\hat{y}_i$ the fitted value obtained from the regression and $\bar{y}$ the mean value of the real-value responses.

Table 9: R^2 and $R^2_{adjusted}$ of the multiple linear regressions.

Regression	50 Hz	100 Hz	150 Hz	200 Hz	250 Hz	300 Hz	350 Hz	400 Hz
$\mathbf{R^2}$	0.98	0.98	0.99	0.99	0.98	0.98	0.96	0.96
$\mathbf{R^2_{adjusted}}$	0.98	0.98	0.98	0.98	0.97	0.97	0.95	0.95

A genetic algorithm (GA) is then used to evaluate the optimum combination of parameter that ensure to maximize the TL of the DOC in the prescribed frequency range. The GA is a method for solving both constrained and unconstrained optimization problems that is based on natural selection, the process that drives biological evolution. GA can be used to solve a variety of optimization problems that are not well suited for standard optimization algorithms, including problems in which the objective function is discontinuous, non-differentiable, stochastic, or highly nonlinear. The GA repeatedly modifies a population of individual solutions. At each step, the genetic algorithm selects individuals from the current population to be parents and uses them to produce the children for the next generation. Over successive generations, the population "evolves" toward an optimal solution. The flow chart reported in Figure 38 outlines the main algorithmic steps.

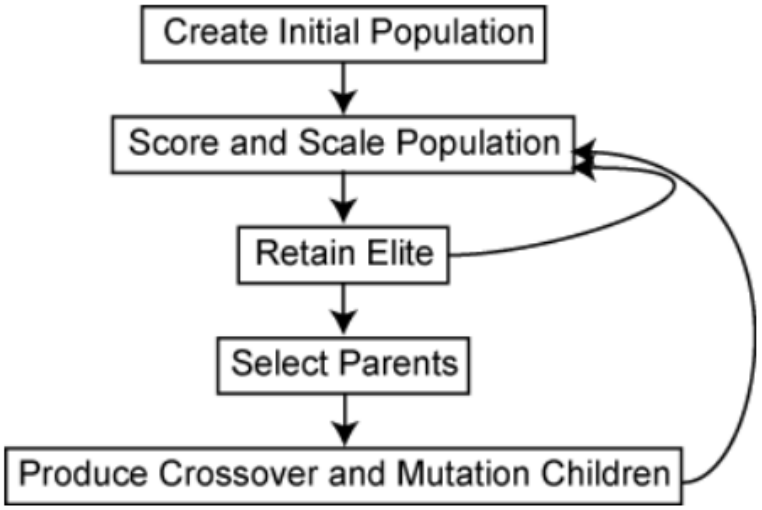

Figure 38: GA main steps.

The GA creates three types of children for the next generation:

- *Elite*, are the individuals in the current generation with the best fitness values (i.e., value of the fitness function for that individual);
- *Crossover*, are created by combining a pair of parents;

- *Mutation*, are created by introducing random changes to a single parent.

The algorithm stops when one of the stopping criteria is met (e.g. fitness function for the best point in the population is less than or equal to a certain limit, the maximum number of generations is reached, maximum time of computation is reached, the average relative change in the fitness function value is less than a certain value, …)

The optimization procedure is implemented with a Matlab script, an Augmented Lagrangian Genetic Algorithm (ALGA) is applied to solve nonlinear constraint problems. The optimization problem solved by the ALGA algorithm can be expressed as follows:

$$\min_{x} \boldsymbol{f}(\boldsymbol{x}) \qquad \textbf{Eq. 30}$$

such that:

$$\boldsymbol{c_i}(\boldsymbol{x}) \leq \mathbf{0} \qquad \textbf{Eq. 31}$$

Where *f(x)* is the objective function and $c(x)$ represents the nonlinear inequality constraints.

In the presented case, the optimization process aims at maximizing the TL in the frequency range of interest. To this end, the area under the TL curve is selected as representative objective function of the stated problem, with the additional constraint that the TL cannot be less than 25 dB. The frequency range of interest is that from 10 to 400 Hz, where the engine noise is more influent (see Appendix 6). The marine silencer typically ensures a sound abatement of about 30-35 dB, so a limit of 25 dB for the TL of the DOC is chosen since, in the real case scenario, it would be mounted in series with a scrubber; so that the abatement of 30-35 dB has to be ensured by the whole system and not only by the DOC that otherwise would result over dimensioned.

In Figure 39 the convergence diagram of the GA used to find the optimum solution is reported.

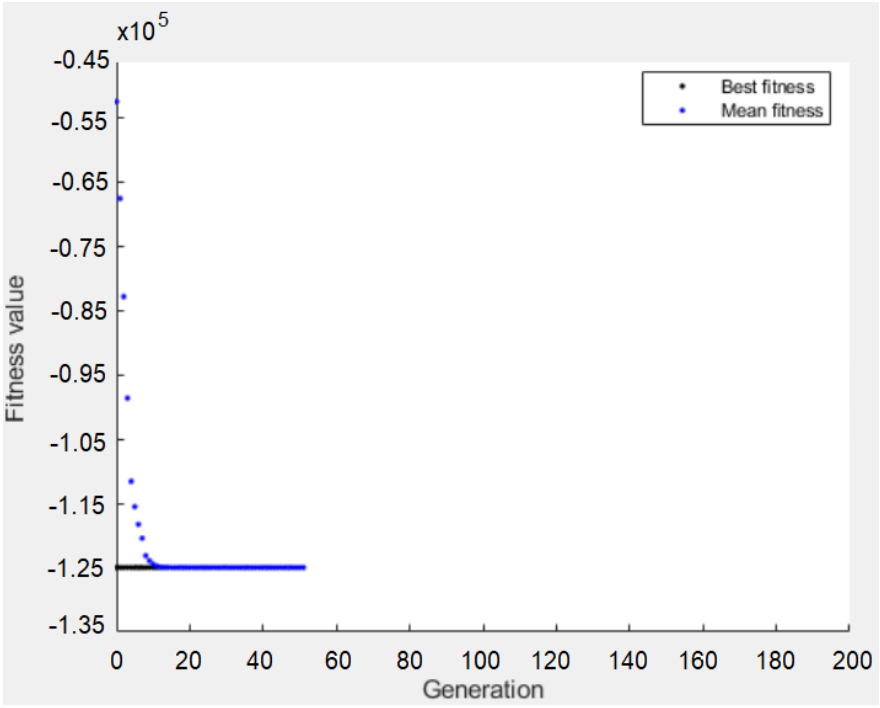

Figure 39: Convergence history of genetic algorithm.

The optimum parameters are reported in Table 10, while in Figure 40 the comparison between the reference TL of the standard DOC and the optimized TL is reported.

Table 10: Optimum combination of parameters to maximize the TL of the SCR.

D [mm]	Θ [deg]	L [mm]	l [mm]	i [mm]	np [-]	R [N·s/m^3]	OAR [-]	Lf [mm]
297	0	510	180	120	0	678	0.92	0

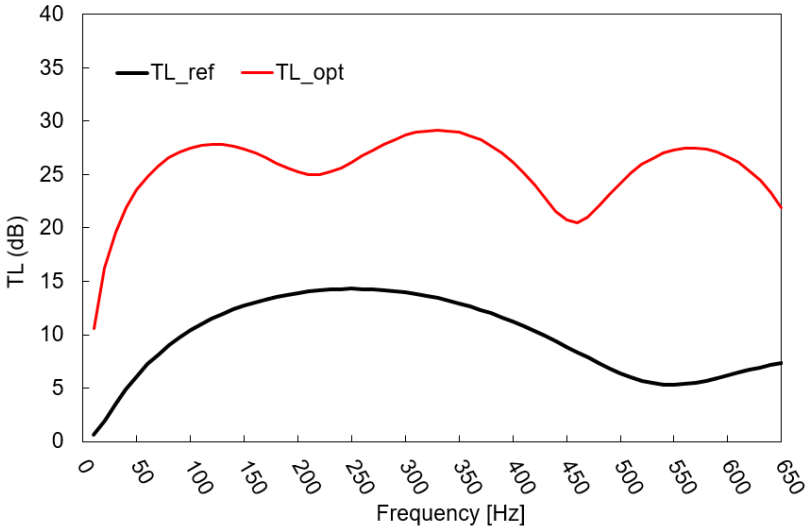

Figure 40: Comparison between optimized and reference TL.

5. Acoustic Performances of DOC and Scrubber in Series

The overall acoustic performance is simulated by considering the optimized DOC located prior to the scrubber (Figure 41) using the model-scale tower packing scrubber (Figure A3-VII). To improve the TL of the scrubber, two perforated steel sheets with conical shape (Figure 42) are inserted under each packing stage. In Table 11 the geometrical parameters are summarized.

Table 11: Summarizing geometrical parameters for the tower packing model scrubber.

D inlet/outlet [mm]	D chamber [mm]	L inlet/outlet [mm]	L chamber [mm]	H inlet [mm]	H conical adapter [mm]	Distance between fillers [mm]
88.9	202	100	1090	150	100	200
H first filler [mm]	**R [N·s/m3]**	**OAR [-]**	**H perforated steel cone [mm]**	**d perforations [mm]**	**holes spacing [mm]**	**Tickness [mm]**
250	520	0.98	150	10	15	3

The proposed CFD-FEM approach is used to evaluate the TL of the integrated system. The TL curves of the single components and that of the whole apparatus are reported in Figure 43. A TL up to 50 dB with minima above 30 dB is ensured in the whole frequency range of interest. Also important is that the minima of the TL do not coincide with the engine firing frequency. In this regard, it is important to stress that an accurate detection of a system's fundamental frequencies is of paramount importance as the f_{min} are the so-

called transparent frequencies and they do not reflect the sound waves backwards, but allowing them to propagate unaltered through the component, leading to null sound attenuation at the outlet. As such, to reduce the exhausted gas noise, these frequencies must not coincide with the engine frequencies.

Considering that the sound attenuation usually developed by marine silencers is around 30-35 dB, the obtained result in terms of TL indicate the feasibility of elimination of the silencer from the exhaust line of the Genset Iveco (Appendix 6). This results in a space saving in the funnel, allowing an easier installation of emission control devices (i.e., DOC and scrubber). Notably, such a configuration of exhaust line, in principle accomplishes both noise and chemical emissions (e.g., PM, HC, SOx and NOx). The back pressure generated by such exhaust line configuration creates a back pressure of 4510 Pa, that is less than the maximum allowable back pressure for the Genset Iveco (4900 Pa). Clearly the use of a fume extractor would be recommended.

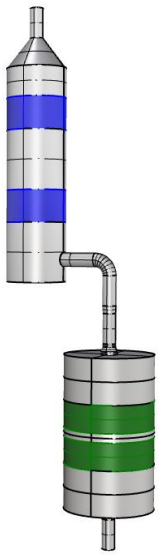

Figure 41: Layout of the exhaust line with DOC and scrubber in series.

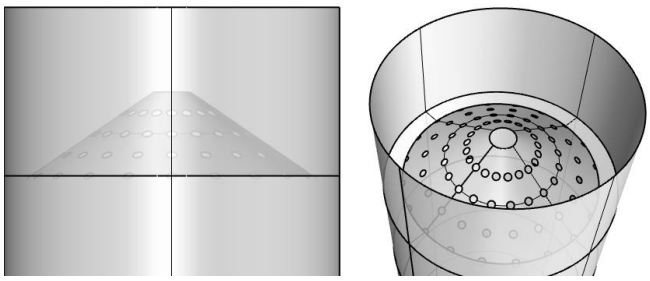

Figure 42: Particular of the perforated cone inside the scrubber.

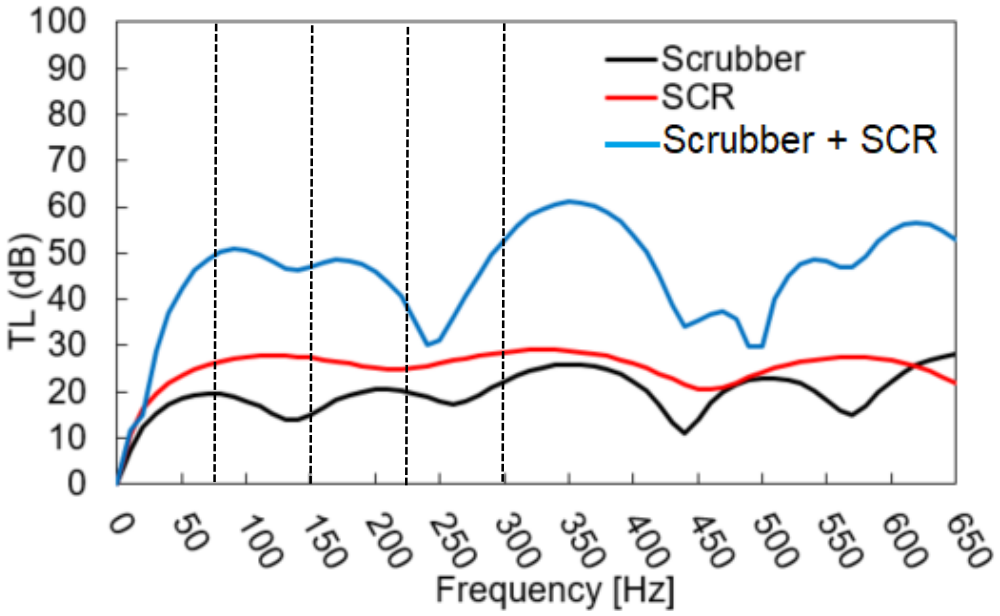

Figure 43: TL of the exhaust line component, in series and alone.

Chapter 5

Conclusion and Future Developments

The present study addresses the development of an effective calculation framework based on numerical methods capable of properly model and optimize the acoustic properties of exhaust line components coupled to a marine diesel engine. The methodology combines scientific methods such as CFD and FEM simulations and GA optimization to provide solutions for the design of the marine engines exhaust systems, combining several after-treatment devices and focusing on reducing the exhaust gas noise and minimizing the exhaust gas system volume, without reducing the efficiency of chemical pollution abatement (i.e., SOx and NOx).

The novel combined CFD-FEM methodology provides reliable results under realistic conditions as it considers the influence of the exhaust flow, while keeping the computational effort reduced. In the first instance, the CFD-FEM approach is assessed using literature data or experimental measurements performed with an impedance tube on simplified geometries (i.e., simple expansion chamber, straight tube perforated muffler). Preliminary studies have been performed to analyze the influence of mesh typology and dimensions on the numerically evaluated TL and to compare different approaches to model porous, perforated and narrow channel components, considering different aspects of dissipations inside such materials. The goal of these investigation is to find a model capable of providing reliable results while keeping a reasonably reduced computational time.

The study is then extended to real industrially relevant systems such as DOCs and scrubbers. The combined CFD-FEM simulation allow to evaluate the acoustic properties (i.e., TL) of such systems, the generated back-pressure and the velocity/pressure field inside the components. This latest aspect is of paramount importance also from a chemical point of view: the possibility to evaluate areas where vorticities are generated leading to a non-homogenous flow on components useful for chemical reactions (e.g., perforated plates, narrow channel components, …) allows to optimize the geometrical design of the cleaning system with an increase in abatement efficiency. The back pressure has to be less than a certain value, dictated by the engine connected to the exhaust line, in order to not reduce the efficiency of the diesel engine. The TL evaluated for the DOC with the

combined CFD-FEM methodology well fits with experimental measurements performed on a diesel Genset mokeup, underlining the potentiality of the proposed approach even if it adopts some simplification, for example the surface roughness. This parameter influences the performances of after-treatment systems and is affected by deposits that occur during operational conditions of the engine. To proper consider the influence of surface roughness and its increase over time, an in-depth study and measurements sets have to be performed also on board in operational conditions.

Finally, the GA optimization is applied to the DOC: the optimum combination of geometrical parameter that maximize its TL is evaluated. The optimized DOC, in series with a model-scale tower packing scrubber, allows to eliminate the silencer along the exhaust line of the Genset used for experimental measurements. This result discloses the possibility of eliminating the silencer thus saving space in the funnel where the spaces are limited, and the installation of after-treatment systems is challenging.

The proposed methods and results are applicable in the maritime industry for the design of marine exhaust line: during the design phase, thanks to its low computational effort and relative easy usage, the proposed methodology allow the study of system integration and the optimization of acoustic properties, leading to the design of an exhaust line with lower volume and compliant with the even more stringent emissions regulations. This aspect is of paramount importance not just for the design of new ships, but also for the refitting of the ships already in navigation. Emission regulations involve also old ships and the possibility to study a system integration that allow to install the needed after-treatment systems in the available space, allow to not perform a refitting of the entire propulsion system.

In the available literature there is a lack of study and general guidelines on the evaluation and optimization of acoustic properties of after-treatment systems used in marine exhaust lines such as scrubbers or catalytic converters. Just few works consider the acoustic properties of SCR, but under simplified hypothesis (e.g., no flow influence, no viscous dissipation inside components) that can lead to a non-negligible discrepancy with a real case scenario. Marine industry is moving to systems integration, for example prototypes of integrated SCRs-silencers have been already constructed, thus the methodologies and results presented in this thesis contribute to the generation of new knowledge that can be used for the optimal design of after-treatment systems. The numerical methodology and

the optimization procedure are proven to be applicable for the study of acoustic properties of after-treatment systems, also considering the geometrical constraints dictated by the chemical aspects. Moreover, the preliminary studies are able to give guidelines on mesh settings and simplified approaches (e.g., porous baffle interface, porous region, rigid porous component, visco-thermal component, transfer impedance) to model internal components such as perforated plates and narrow channel components.

The combined CFD-FEM approach presents some limits due to the adoption of simplified models such as steady state CFD simulations for the evaluation of flow field and the above mentioned strategies to model internal components without the need to design and mesh their exact geometry. Moreover, parameters such as surface roughness, that in the real case scenario influence the performances of the after-treatments systems, or the water spry inside the scrubber are not considered. On the contrary, the methodology does not require the knowledge of parameters difficult to estimate with measurements, thus the above mentioned approximations, while leading to a discrepancy with a real case scenario, allow to have a methodology capable of predict acoustic properties of after-treatment systems, study their integration and optimize their performances and volumes also in an early design stage. Of paramount importance, especially for the application in industrial sectors, the proposed methodology have a low computational effort.

In future the optimization process should be applied to whole system (i.e., DOC plus real scrubber) to further optimize the design, volumes and operation conditions.

Moreover, the influence of water spry inside the scrubber on the acoustic properties should be evaluated. As for the noise generated by the exhaust gas itself, preliminary simulations using SNGR suggest that the noise generated by flow turbulence is limited to high frequencies and tends to be a local phenomenon (i.e., not carried by the gases up to the exit of the funnel and radiated to the outside). However, further investigation should be performed to properly assess this aspect.

Finally, an interesting study can be represented by the optimization of probes used for in-duct measurements of exhaust gas noise. The test conditions are difficult (e.g., temperature, particulate matter, flow turbulence, …) and ad hoc sensors should be developed to obtain more reliable results and improve also their durability.

Appendix 1

A Preliminary Study to Optimize CFD Simulations

During the design of the exhaust line, the evaluation of the acoustic properties of key components such as silencers is performed by numerical analysis. However, in the literature, there is a lack of general guidelines and comparisons among different modelling strategies. So, in this preliminary study [29], the influence of grid type (i.e., trimmed vs tetrahedral) and dimension on the numerical prediction of the flow inside a reactive silencer is analyzed.

The study uses as reference geometry the silencer reported by [71] with an OAR equal to 1 (Figure A1-I).

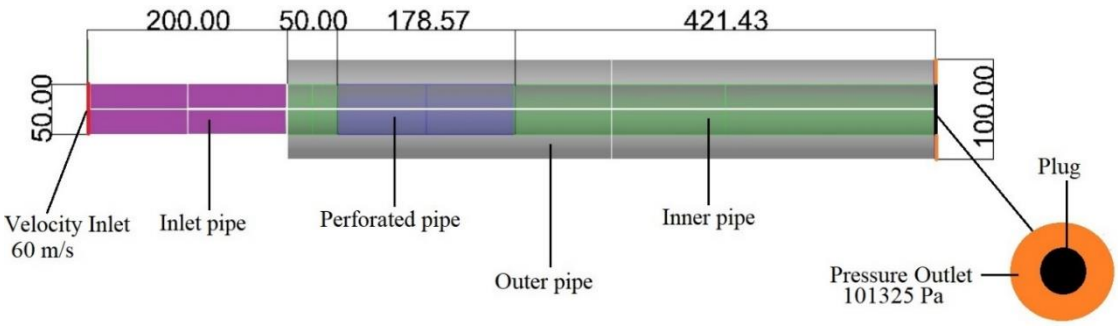

Figure A1-I: Literature geometry used for preliminary study.

A literature study, that reports both experimental and numerical data, is used as reference because during the preliminary study the experimental set-ups and prototypes in our laboratories were not ready yet.

The software STAR-CCM+ is used to perform the CFD analysis. All the physical parameters and the boundary conditions are set following the case study chosen [71] to use the literature data as reference to evaluate the obtained results by the present study [29].

A segregated and steady approach is used in the framework of the RANS (Reynolds Averaged Navier Stokes) simulations in combination with the k-ε turbulence model.

The domain is discretized with both tetrahedral and trimmed meshes using a base size chosen on the basis of the mesh sensitivity study presented following. The prism layer is generated with a total thickness of 5.83 mm and 6 prism layers with a stretching factor of

1.5 in order to obtain a wall $y^+ \leq 1$. A refining area is set around the perforated pipe, setting a target value of 20% of the base size for the generated cells.

1. Mesh sensitivity study

The mesh sensitivity study is performed with both the tetrahedral and the trimmed mesh. The pressure drop (ΔP) between the inlet and the outlet is chosen as the reference parameter and the base size is varied in the range of 1.25-20.00 mm with a refinement ratio equal to 2. The asymptotic solution can be evaluated by the GCI (Grid Convergence Index) [72], expressed in the following equation:

$$GCI = 1.25 \left\{ \left({}^{|F_{i+1} - F_i|}/_{F_i} \right) \left[{}^{1}/_{(r^p - 1)} \right] \right\} \qquad \textbf{Eq. A1-I}$$

where r is the refinement ratio, F_i is the model values with i decreasing with the grid refinement and p is the solution convergence order expressed in the following equation:

$$p = {}^{ln\left({}^{F_{i+2} - F_{i+1}}/_{F_{i+1} - F_i} \right)}/_{ln(r)} \qquad \textbf{Eq. A1-II}$$

Comparing two successive values of *GCI* using the following equation, the asymptotic solution can be estimated: when the value of the parameter A_r is near to 1, the desired condition is satisfied.

$$A_r = r^p \left({}^{GCI_i}/_{GCI_{i+1}} \right) \qquad \textbf{Eq. A1-III}$$

A perusal of Figure A1-II shows that by decreasing the cell dimensions, the calculated ΔP reaches convergence. A value of Ar equal to 1.0 is obtained considering GCI2.5 and GCI5 for both the tetrahedral mesh and the trimmed one [28]. Accordingly, a mesh size of 5.0 mm is selected for the computations as it is in the asymptotic range and it represents the best compromise between computational cost and the accuracy of the results.

Appendix 1

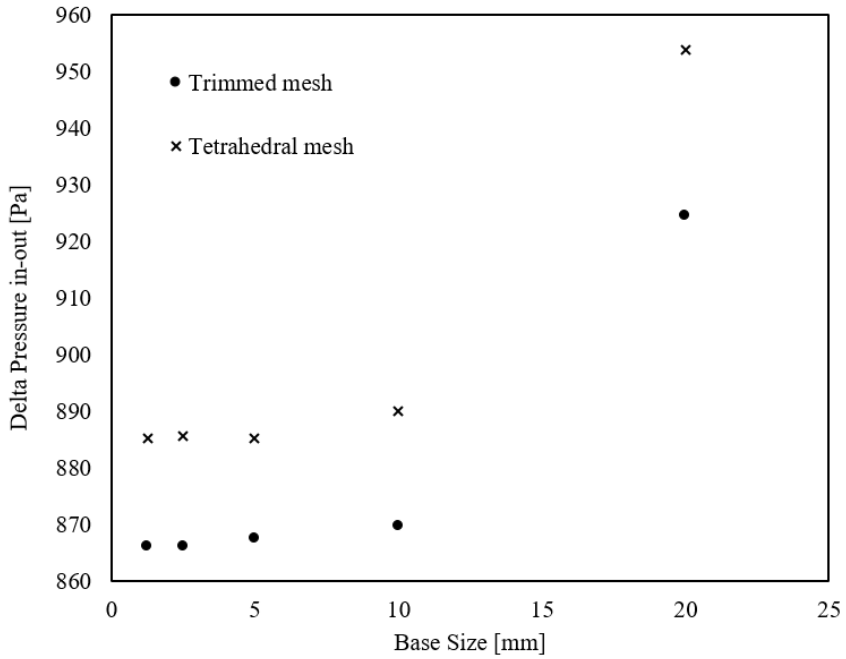

Figure

2. Results and discussion

To

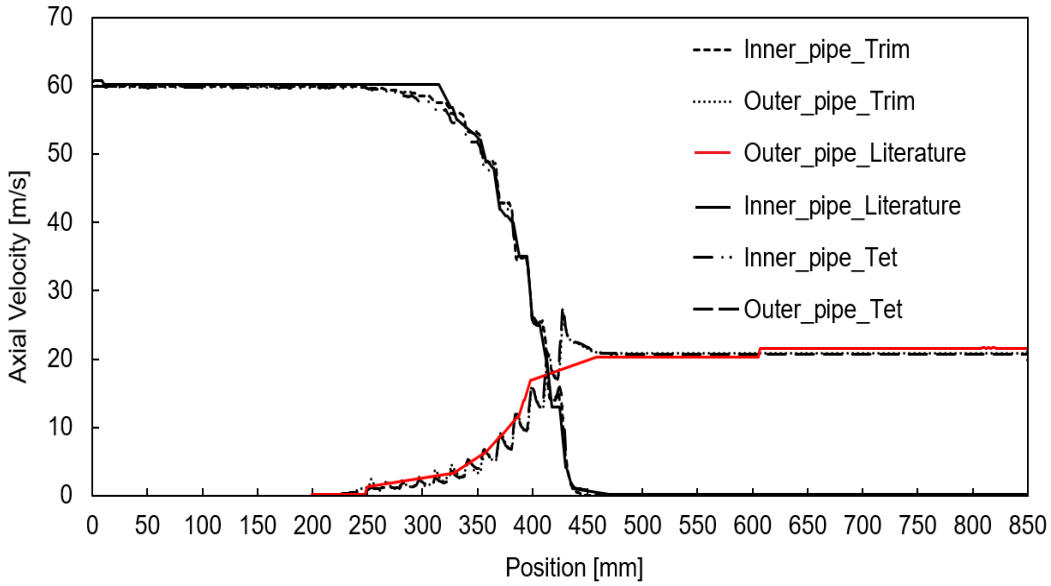

Fig.

The

The

Error!

Appendix 1

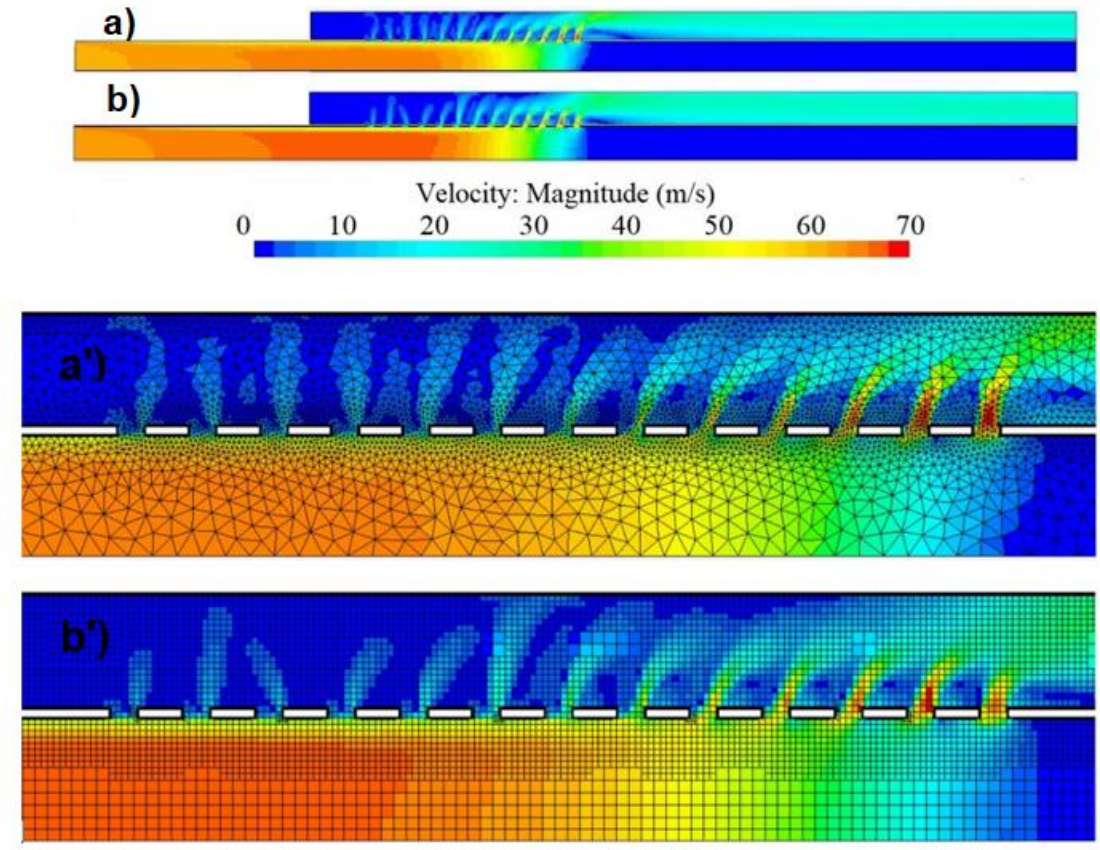

Figure A1-IV: Velocity field with a) tetrahedral and b) trimmed mesh. a') and b') highlight the flow through the holes.

So, considering the small variation in terms of ΔP between the two mesh typology, the lesser computational burden (55% fewer cells and 78% lower CPU time) and the small difference in terms of mesh quality, the trimmed mesh is chosen as the best one.

Appendix

Simplified

This study is performed with the aim to develop a faster approach to model perforated elements, typically used in components such silencers and for which there is a lack in literature of comparison between different modelling strategies. In particular, a comparison between the use of porous baffle interface and porous region to model perforated elements is addressed.

For this study, the same geometry and settings of the simulation are used as those adopted in the preliminary study reported in Appendix 1, whit the addition of resistance parameters needed to use a porous baffle interface and porous region.

1. Resistance coefficients for perforated elements

Considering the Darcy-Forchheimer law ($\Delta \boldsymbol{PL} = -\left(\boldsymbol{\nu\alpha} + {}^{\mathbf{1}}/_{\mathbf{2}}\, \boldsymbol{V\beta}\right)\boldsymbol{V}$), an expression for α and β, that depend on porous media properties such as porosity ε and particle size d_p, was proposed by Ergun [75]:

$$\boldsymbol{\alpha} = {}^{\mathbf{150}}/_{\boldsymbol{d_p^2}}\, {}^{(\mathbf{1}-\boldsymbol{\varepsilon})^2}/_{\boldsymbol{\varepsilon^3}} \qquad \textbf{Eq. A2-I}$$

$$\boldsymbol{\beta} = {}^{\mathbf{1.75}}/_{\boldsymbol{d_p}}\, {}^{(\mathbf{1}-\boldsymbol{\varepsilon})}/_{\boldsymbol{\varepsilon^3}} \qquad \textbf{Eq. A2-II}$$

These expressions are valid for cellular media, made of small sphered shapes particles. To this end, the perforated pipe can be compared to a cellular media, constituted by solid filaments connected to form pores. So, the equivalent particle diameter expressed as follows is used to calculate α and β coefficients [76]:

$$\boldsymbol{d_e} = \mathbf{1.5}\ {}^{\mathbf{1}-\boldsymbol{\varepsilon}}/_{\boldsymbol{\varepsilon}}\ \boldsymbol{d_h} \qquad \textbf{Eq. A2-III}$$

where d_h is the hydraulic diameter of the hole:

$$\boldsymbol{d_h} = \mathbf{4}\, {}^{\boldsymbol{Open\ Area}}/_{\boldsymbol{Wet\ Perimeter}} = \mathbf{4}\, {}^{\boldsymbol{Open\ Volume}}/_{\boldsymbol{Wet\ Area}} \qquad \textbf{Eq.A2-IV}$$

In this work, the only resistance parameter considered for the porous baffle interface is the inertial one, being the flow inside the silencer turbulent (Re~30000).

Appendix 2

2. Results and discussion

Figure A2-I shows the velocity fields along the silencer calculated with the real geometry model and the simplified models. It is immediate to notice how the porous interface/region model does not properly reproduce the flow through the holes as in the real geometry. The porous interface/region is crossed by the flow by their entire length and the resistance to cross-flow is imposed using the resistance parameters. This approximation does not allow for capturing local-flow phenomena such as pressure and velocity fluctuations or vortices.

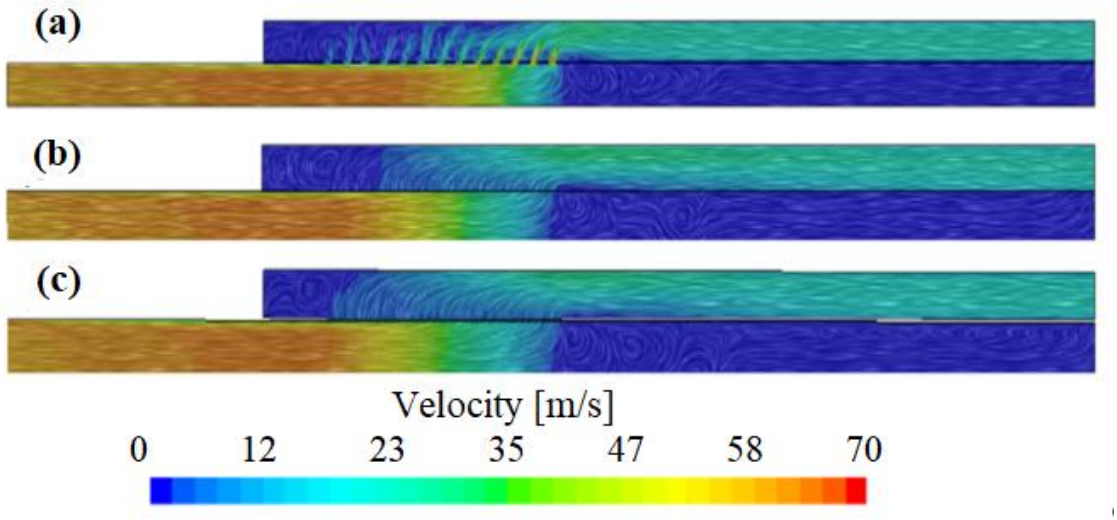

Figure A2-I: Velocity field with streamline calculated along the silencer: (a) real geometry model; (b) porous baffle interface model; (c) porous region model.

The ΔP calculated with the porous baffle interface and the porous region models differ from the value obtained with the real geometry model of about 13% and 12% respectively [74]. It is then possible to affirm that the inertial resistance parameter calculated with Eq. A2-II is not adequate to properly reproduce the effect that the perforated pipe has on the flow.

Considering the computational burden (simulations performed with the same hardware reported in Appendix 1), the reduction in terms of both the number of cells and CPU Time is at most about 14-15 %.

On the other hand, the use of simplified models allows for saving time during the design of the CAD (Computer-Aided Design) model, when possible different values of porosity and hole diameters need to be studied. For example, using a macro, it is possible to

automatically change the parameters of the perforated elements, without the necessity to re-draw and re-mesh the model.

Appendix 3

Experimental set-up with an impedance tube

A simple expansion chamber (Figure A3-I), which represents one of the simplest reactive silencers, is first used to assess the experimental set-up used for the measure of the TL of the prototypes constructed during this research.

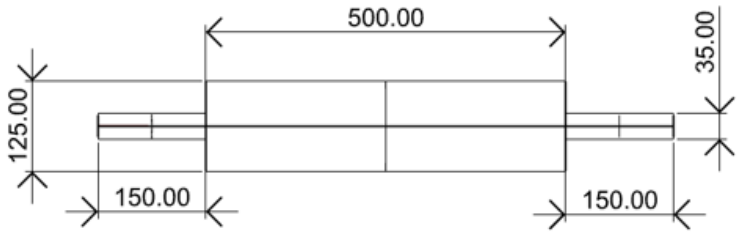

Figure A3-I: Geometry of simple expansion chamber, dimensions in mm.

Its TL can be easily calculated analytically with the following equation:

$$TL = 10log_{10}\left(1 + {}^{1}/_{4}\left(h - {}^{1}/_{h}\right)^{2} sin^{2}(kl)\right) \qquad \textbf{Eq. A3-I}$$

The maxima (f_{max}) and the minima (f_{min}) of the TL curve can be calculated using the following equations, where n is the number of the considered harmonic and l is the chamber length [77]:

$$f_{min} = n\,{}^{c}/_{2l} \qquad n = 0, 1, 2, \ldots \qquad \textbf{Eq. A3-II}$$

$$f_{max} = {}^{c}/_{4l} + n\,{}^{c}/_{2l} \qquad n = 0, 1, 2, \ldots \qquad \textbf{Eq. A3-III}$$

The measurement set-up consists of an impedance tube featuring a diameter of 45 mm. The two-loads technique (Chapter 2) is adopted and the two loads are reproduced using a closed and an open termination (FigureA3-II). The speaker emits a sine sweep with the following parameters: duration of 10 s, frequencies range 50-5000 Hz, variable amplitude between 0.05 V and 0.40 V. The signals are acquired by two PCB Piezotronics 378C10 microphones connected to a data acquisition device NI USB 4431. Three measurements are performed for each set-up configuration moving microphone 2 to locations 3 and 4

while keeping microphone 1 in its location (see Figure 155). The acquired traces are elaborated to obtain the TL values using the Main_TL software developed by Materiacustica s.r.l. The distance between microphones 1-2 and 3-4 is equal to 30 mm, following the standard ISO 10534-2 [49] that fixes the following limit to the distance *s* between microphones:

$$s < 0.45\ {}^{c}/_{F} \qquad \textbf{Eq. A3-IV}$$

where *F* is the maximum considered frequency. Moreover, a distance between the sample and microphones 2 and 3 greater than 1-2 tube diameters is suggested in the literature [78].

The ISO standard [49] provides also a frequency limit to ensure a plane wave propagation (Eq. 7), in our case the measures are performed up to 1700 Hz.

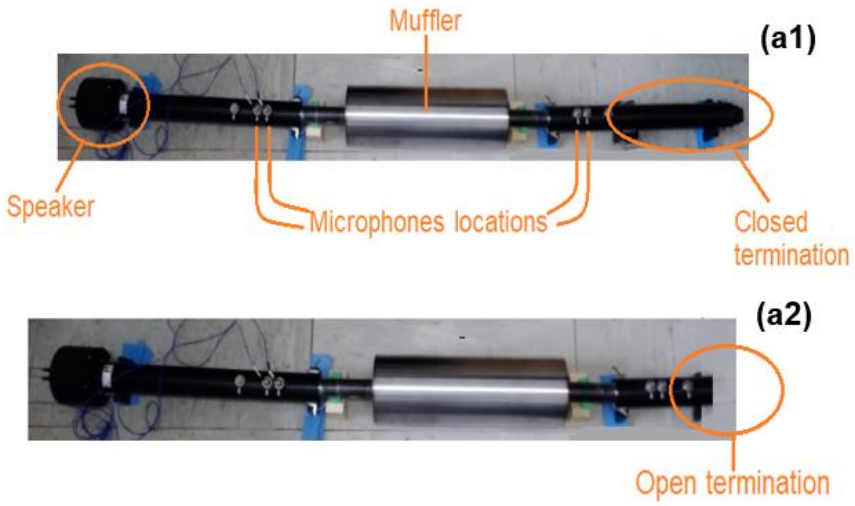

FigureA3-II: Experimental set-up for the measures of the TL with the closed (a1) and the open (a2) terminations.

In Figure A3-III the comparison between the analytical and measured TL of the simple expansion chamber is reported.

Appendix 3

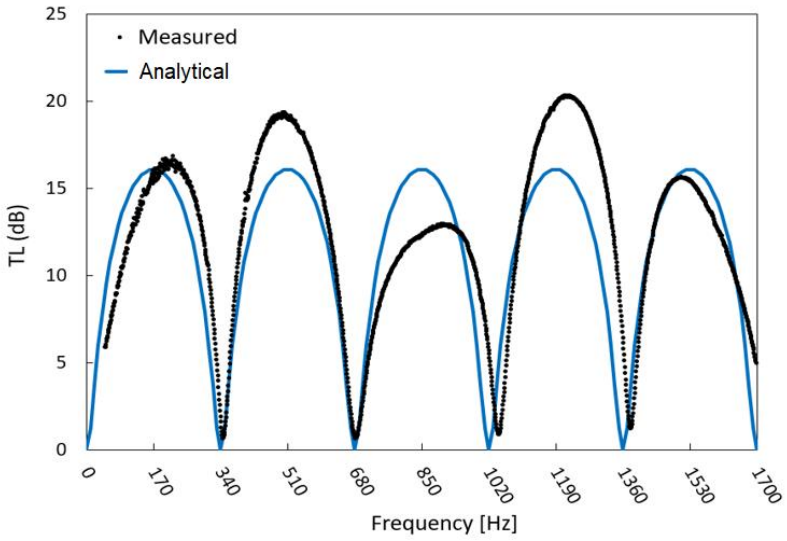

Figure A3-III: Comparison between TL analytical curve and measured TL of the expansion chamber.

As highlighted in the published paper [79] good fitting is reached between analytical and measured f_{min} as the differences are less than 3 %. Instead, more significant are the differences in terms of amplitudes: these discrepancies can be attributed to the discontinuity introduced along the pipe by the bushing with O-rings (FigureA3-IV) used to connect the expansion chamber and the impedance tube. This solution ensures airtightness of the system, facilitating the assembly of the setup, but creates a discontinuity along the pipe that influences the measurements. The effects of this geometry setup on the TL is analyzed using the FEM model (Appendix 4).

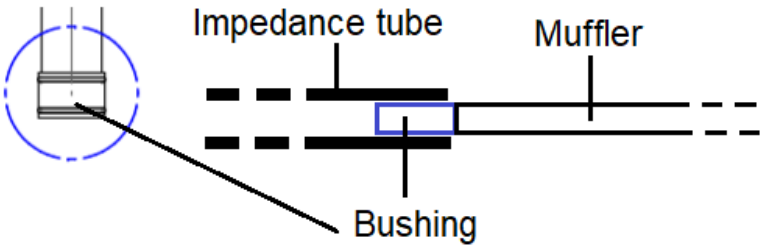

FigureA3-IV: Details of the bushing used to connect the expansion chamber and the impedance tube.

The presented measuring set-up is used to evaluate the TL without the presence of flow also of the following prototypes: a model-scale scrubber with perforated plates 1 mm thick with holes featuring a diameter of 6 mm and a holes spacing of 9 mm (FigureA3-V); an DOC with two metallic catalysts with 300 sinusoidal cells/inch^2 (Figure A3-VI); a

model-scale scrubber with two tower packing composed by corrugated channels inclined at 45° (Figure A3-VII).

To notice is that the conical adapters used to reduce the inlet/outlet diameter of the DOC and the model-scale tower packing scrubber (Figure A3-VI and Figure A3-VII) down to that of the impedance tube modify the TL of the component. This influence is highlighted with the use of the FEM model (Appendix 4).

Moreover, the model-scale scrubber with perforated plates is experimentally tested without the water at the bottom (FigureA3-V), its influence on the TL is investigated with the assessed FEM model (Chapter 4).

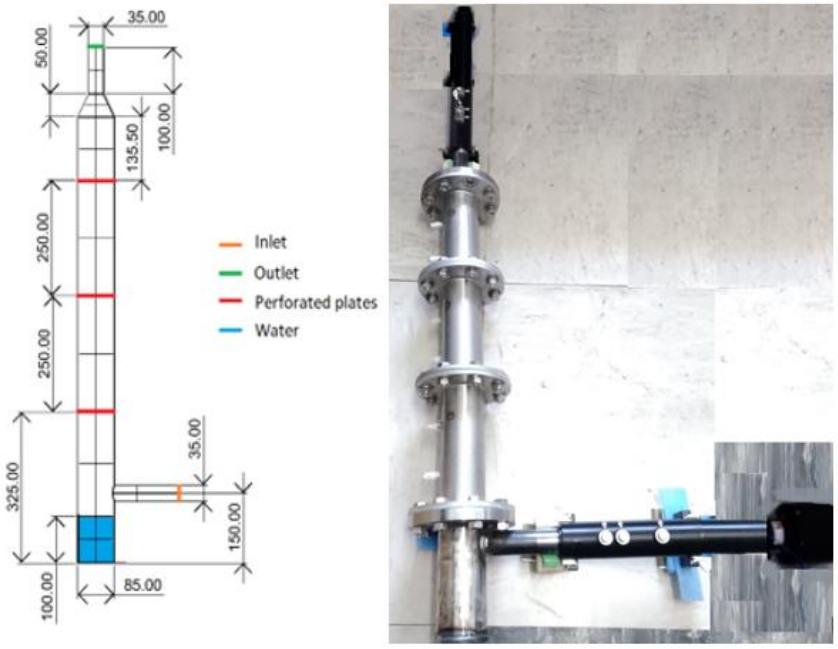

FigureA3-V: Model-scale scrubber with perforated plates.

Appendix 3

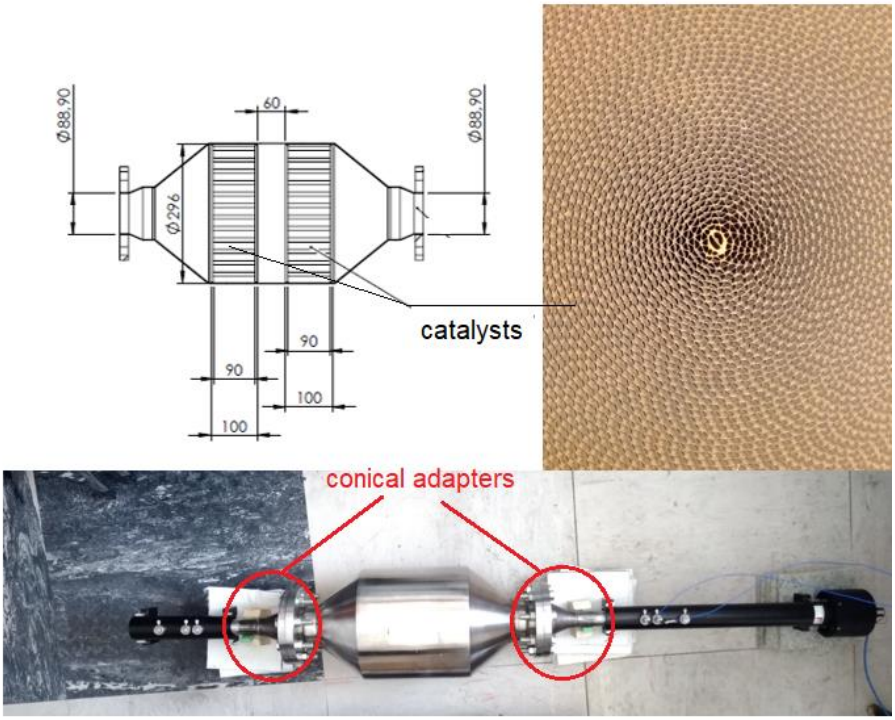

Figure A3-VI: DOC with metallic catalyst composed of sinusoidal shape narrow channel.

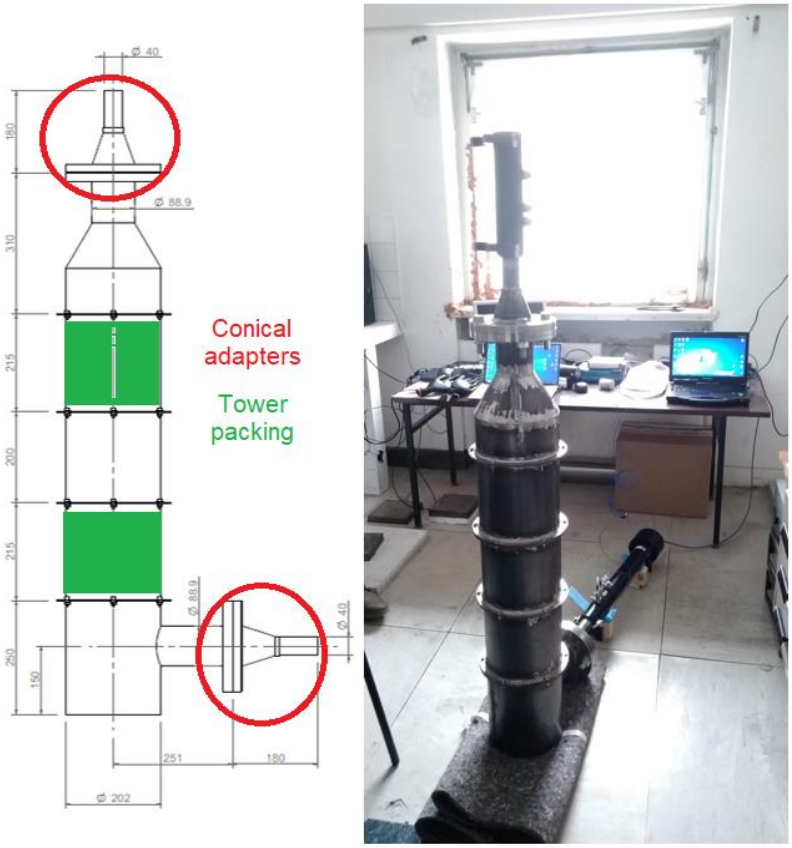

Figure A3-VII: Model-scale scrubber with tower packing.

Appendix 4

Assessment of the FEM model

The FEM model is assessed by comparison with the experimental results obtained for the simple expansion chamber. The assessed model is then used to investigate the effects on the TL of the bushing (FigureA3-IV) and the conical adapters (Figure A3-VI). Finally, the influence of the water at the bottom of the scrubber (FigureA3-V) and of some geometrical modifications on the model-scale scrubber TL is investigated [79].

The numerical simulations are performed using the software Actran VI [50], implementing a Direct Frequency Response analysis. The geometries are discretized with the Actran mesh generator. First, the surfaces of the studied geometries have meshed, and then the volume mesh is generated starting from the meshed surface to discretize the interior volume. A tetrahedral mesh is used and the mesh size is chosen following the guidelines [50,80,81], basing on the maximum frequency analysed, 10 linear elements per wavelength are set. The boundary conditions are set as explained in Section 1 of Chapter 3, imposing a plane wave propagation. In this regard, the simulations are performed up to the frequency limit that ensures these conditions (Eq.7). Perforated elements are modelled by applying a transfer impedance, the filler using the rigid porous component (Chapter 3, Section 1.2), while the catalyst is modelled with both rigid porous component and visco-thermal component (Chapter 3, Section 1.2). The fluids characteristics (i.e., air and water) and material properties (i.e., density, Young modulus, Poisson coefficient) are set under the same ambient conditions during the experimental measurements [79].

1. Simple expansion chamber

Figure A4-I compares the analytical (calculated with Eq.A3-I) and numerical TL values as a function of frequency for the simple expansion chamber (Figure A3-I).

Appendix 4

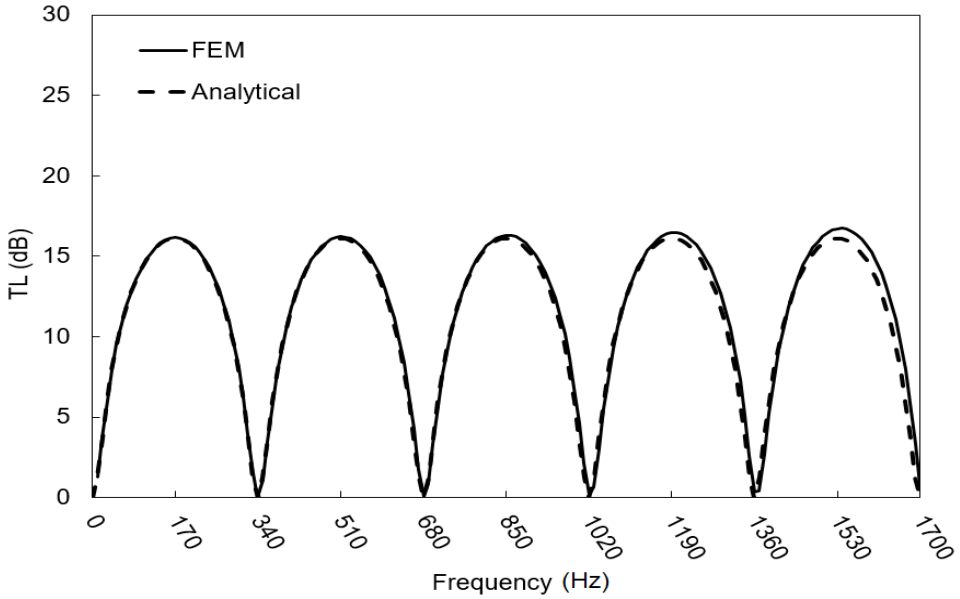

Figure A4-I: Comparison between numerical and FEM-simulated TL of the expansion chamber without tube discontinuity.

The analytical curve is nearly coincident with the FEM-simulated TL of the simple expansion chamber: frequency differences much lower than 1% and amplitude differences lower than 1 dB [79].

After comparing the numerical model against analytical data, the discontinuity along the tube caused by the bushing is modelled considering a sudden change in diameter from 35 mm (prototype pipe diameter) to 45 mm (impedance tube diameter).

A comparison of Figure A4-II and A-II clearly shows that the irregular features of the experimental amplitudes are caused by the connection between the chamber and the impedance tube.

Appendix 4

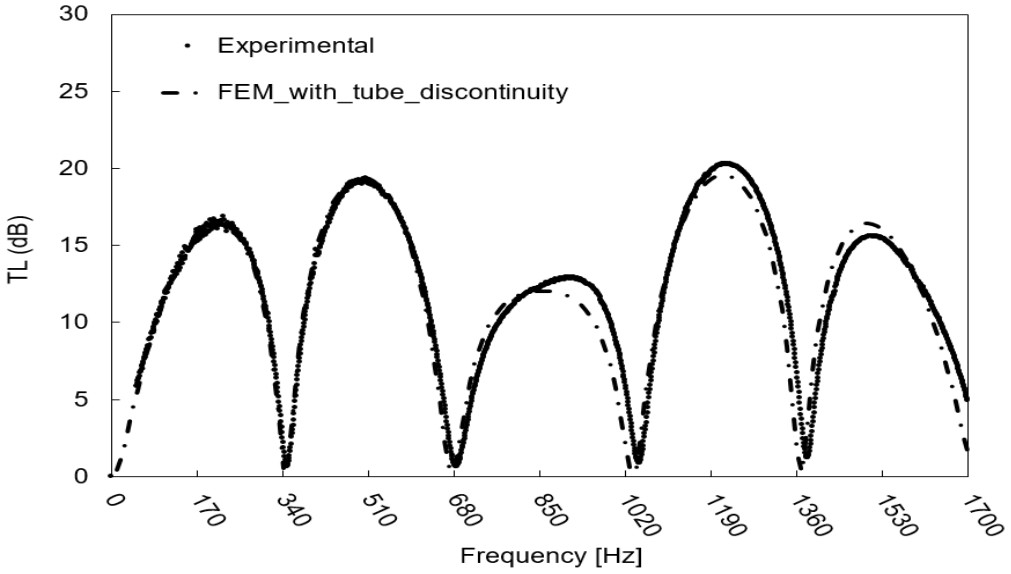

Figure A4-II: Comparison between experimental and FEM-simulated TL of the expansion chamber with tube discontinuity.

In fact, a very good fitting between experimental and calculated TL using the model which includes the tube discontinuity: the differences in f_{min} value and amplitude are less than 1% and 1 dB, respectively [79].

2. Model-scale scrubber with perforated plates

The simple FEM model is extended to simulate the TL of the model-scale scrubber (FigureA3-V). Considering the model of the scrubber with the tube discontinuity, a perusal of Figure A4-III shows a good fitting between the FEM-simulated and experimental TL curves in the frequency range up to 1500 Hz, where the discrepancy between f_{min} is less than 3% and between amplitudes is less than 5 dB [79]. At higher frequencies, the discrepancy between TL amplitudes becomes higher. This inaccuracy is caused by a no plane wave propagation of the sound at higher frequencies in the model-scale scrubber due to a change in the wave propagation direction caused by the angle between the inlet pipe and scrubber body [82]. In this regard, it should be remembered that the hypothesis of plane wave propagation is adopted both in the experimental measurements and in the numerical model.

Appendix 4

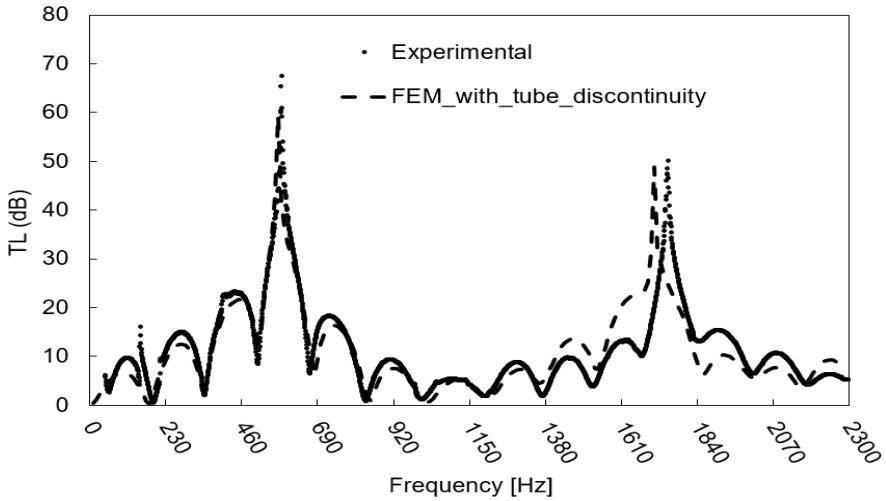

Figure A4-III: Comparison between experimental and FEM-simulated TL of the model-scale scrubber with discontinuity.

However, the FEM model shows appreciable accuracy in the frequency range 20-1000 Hz, in which the human hearing is most sensitive [83] and taken as a reference by industry. Therefore, the assessed FEM model can be employed to analyse the effects of scrubber modifications (e.g., water presence or geometry modifications) on the TL.

For this purpose, the model-scale scrubber without tube discontinuity is firstly modelled, to avoid the influence of such discontinuity on the TL (Figure A4-IV). The model is then used to study the influence on the TL of the presence of water (generated by the water spraying on the perforated plate involved in the chemical processing of the exhaust gases to reduce emissions) in the model-scale scrubber bottom (depicted in FigureA3-V). The TL peak around 500 Hz is completely dumped, while the TL above 920 Hz is increased (Figure A4-IV). This result stresses the importance of the necessity of modelling the system under realistic conditions and the effect clearly should be kept present when interaction with exciting frequencies is considered.

Appendix 4

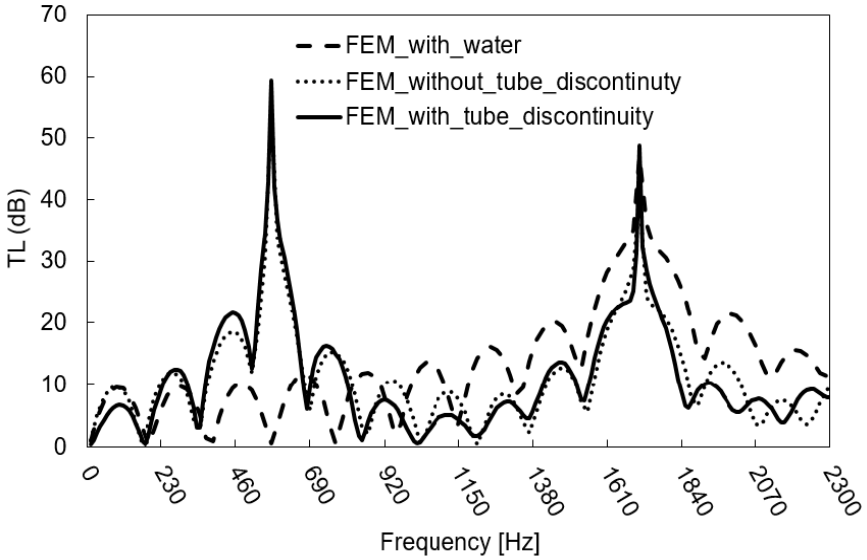

Figure A4-IV: Comparison between experimental and FEM-simulated TL of the model-scale scrubber with and without discontinuity and with water without discontinuity.

Regarding the geometry modifications, they hopefully have to increase the TL values, since higher TL values correspond to higher sound attenuation.

The basic design of the scrubber (i.e., characteristics of the perforated plates and scrubber diameter and height) should comply with the requirements of the chemical processing of exhaust gases and cannot be modified to improve the acoustic performance of the component. So, the influence on the TL of modifications that do not modify the chemical process, such as the inlet/outlet pipes diameter and length, are investigated using the assessed FEM model without tube discontinuity, which in the real case scenario are not present. The obtained results are fully illustrated in [79].

More evident and interesting is the influence on the acoustic performance of the insertion of elements as perforated pipes or filler (Figure A4-V). The perforated pipes are 1.5 mm thick with holes featuring a diameter of 4 mm. The hole spacing is 8 mm. The filler has a flow resistivity of 3000 $Pa \cdot s/m^2$, typical of a rigid metal foam. Moreover, the water at the bottom of the scrubber is removed as a water drain can be added to the scrubber to increment the TL without influencing the chemical properties.

Appendix 4

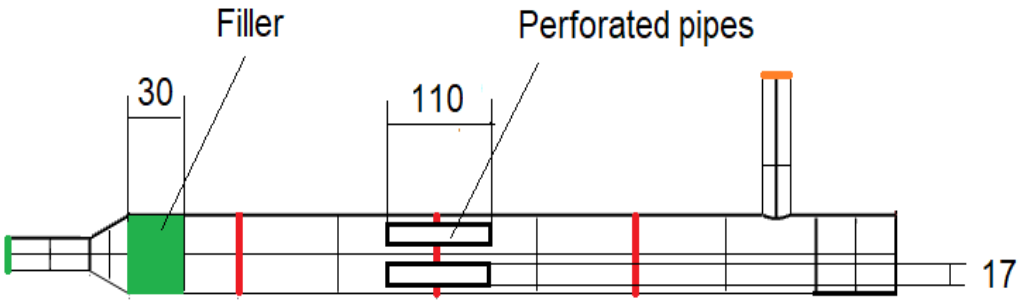

Figure A4-V: Model-scale scrubber geometry modifications.

A perusal of Fig. A4-VI shows that the insertion of the perforated pipes not only increases the TL amplitudes but also changes the fundamental frequencies of the system; this aspect has to be taken into account when the coupling with the engine is studied as the transparent frequencies with the exciting ones must be avoided. The filler insertion improves the TL and changes its features due to the viscous dissipation generated by the passage of the sound wave through its porous structure. The simultaneous addition of filler and perforated pipes further increases the TL, coupling the dissipation effects of the porous structure and the holes. These preliminary results demonstrate the validity of using the proposed FEM model to investigate the acoustic properties of different geometry configurations.

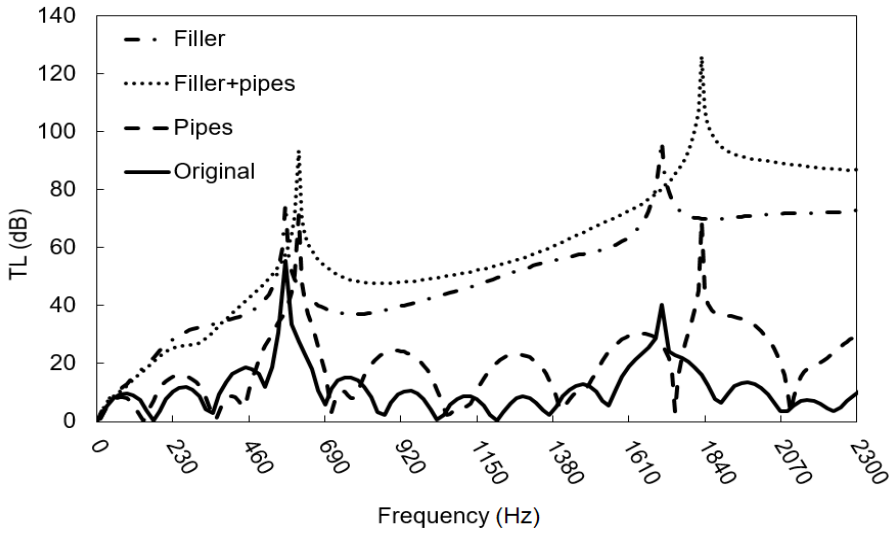

Fig. A4-VI: Influence of the insertion of a perforated pipe and filler on the model-scale scrubber TL.

Appendix 4

3. DOC

The analysed DOC (Figure A3-VI), before being mounted on the exhaust line of the Genset (Figure A6-I), is tested with the impedance tube. The measured TL is compared with numerical data (Figure A4-VII) obtained with the FEM model, using both rigid porous component (rpc) and visco-thermal component (vtc). The flow resistivity is calculated with Eq. 14, using the hydraulic radius of the sinusoidal shape of the catalyst channel (Eq. 22), obtaining a value of 430 N·s/m^4. The vtc model fits better the experimental TL curve, especially in the frequency range of interest (10-400 Hz where the engine noise is more influent, see Appendix 6), compared to the other models. Accordingly, this model is chosen for the following computation.

Thanks to the FEM model is possible to evaluate the influence of the conical adapters (Figure A3-VI) used to connect the DOC to the impedance tube. In Figure A4-VII the blue line represents the TL of the DOC without the conical adapters experimentally used for the connection with the impedance tube (Figure A3-VI). This configuration represents the real case scenario of connection of the DOC with the exhaust line of the Genset.

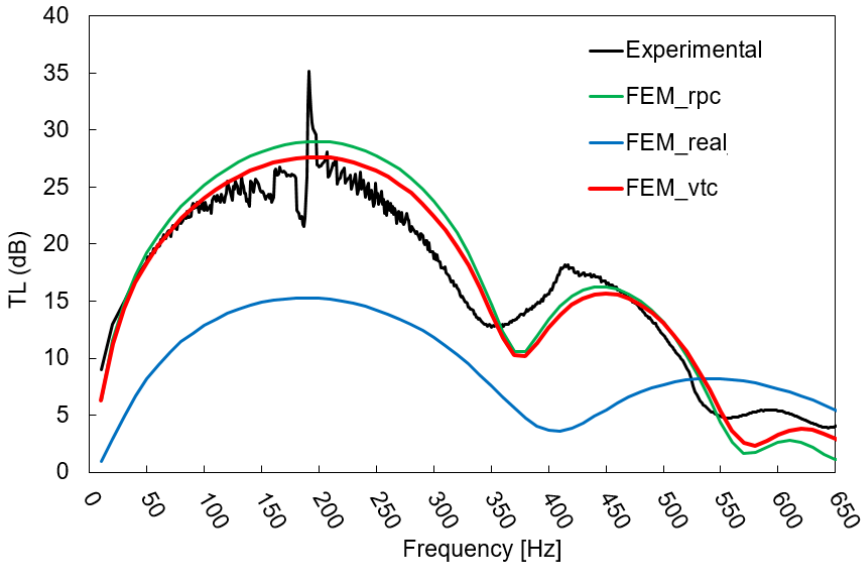

Figure A4-VII: Comparison of TL without flow.

Appendix 5

Assessment of CFD model

The assessment of the CFD model is performed by comparing numerical results and data reported in the literature [28] for a straight-tube perforated silencer (Figure A5-I). A literature case study is chosen for the assessment of the proposed CFD model due to the difficulty to insert and measure the flow in simple geometries in our laboratories. The perforated pipe has holes features holes with a diameter of 6 mm, porosity of 9% and a thickness of 2 mm.

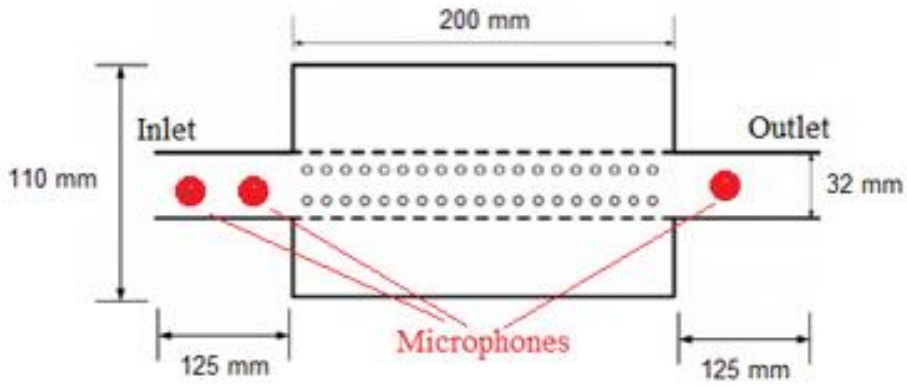

Figure A5-I: Straight-tube perforated silencer geometry.

The software STAR-CCM+ is used to perform the CFD simulations. RANS model is used to solve the Navier-Stokes equations, setting the k-ε turbulence model and considering the working medium air as a compressible ideal gas with physical properties dependent on the temperature [84]. The segregated approach is used, adopting the SIMPLE (Semi Implicit Method for Pressure Linked Equation) and the PISO (Pressure Implicit with Splitting of Operations) algorithms for respectively the steady and the unsteady-state simulations. The time step used for unsteady simulations is $5 \cdot 10^{-6}$ s. The prism layer settings are chosen to have a Wall $y^+ \leq 1$, while the mesh base size and refinement area are generated according to previous studies available in the literature [28]. Figure A5-II reports the discretized geometry.

Appendix 5

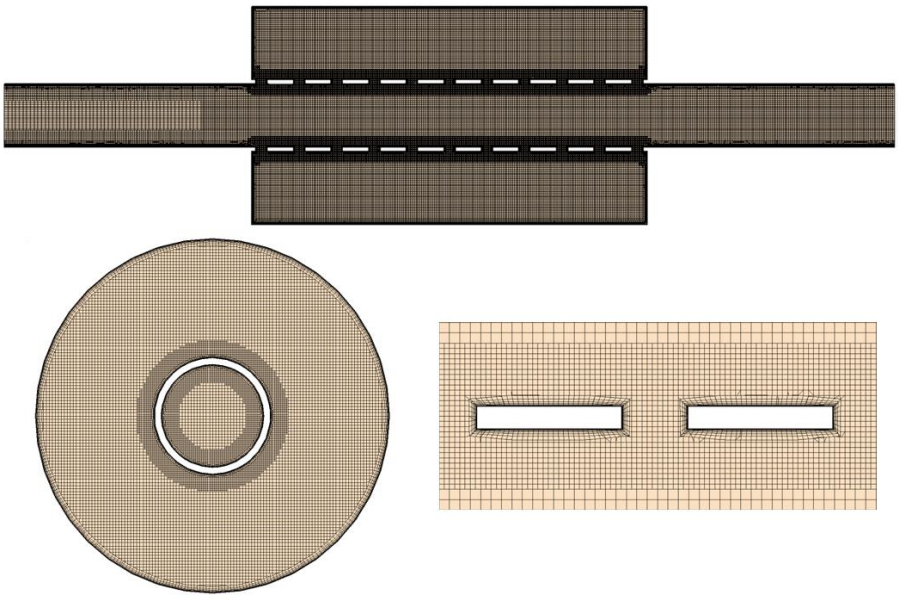

Figure A5-II: Mesh of straight-tube perforated silencer, with particulars of the refinement around the holes and the cross-section.

The boundary conditions are set as follows: mass-flow inlet (41 kg/m2, equivalent to a velocity of 0.1 Ma), pressure outlet (101325 Pa) with an NRBC, no-slip condition at walls and temperatures at 288 K. The perforated pipe is modelled with the real geometries, consistent with the considerations reported in Appendix 2.

For the TL calculation, three microphones have to be set in the model (Figure A5-I) and positioned following ISO standards [49]. The registered signals are then elaborated using the decomposition technique (Chapter 2). For this porpoise, after a steady simulation, two subsequent unsteady simulations are needed, one with the simple mass-flow inlet and another with a half-sine wave impulse superimposed to the constant mass flow, as explained in section 2 of Chapter 3. Residuals in the order of 10^{-5} are chosen as a convergence criterion.

Signal pressures are registered in each measuring point during both the unsteady simulations and then subtract from each other (see section 2 of Chapter 3). The obtained time domain signals (one for each microphone) are converted into frequency domain signals through an FFT code written in Matlab using the following parameters: resolution 0.05 Hz, flat-top window, linear averaging, overlap 50. The decomposition technique formulation (Chapter 2) is then used to obtain the TL curve [85].

In Figure A5-III the TL of the straight-tube perforated silencer calculated with the CFD approach is reported and compared with both experimental data and CFD-modelled TL

reported in the literature [28]. It is possible to notice a good fitting between the curves up to 2450 Hz, at higher frequencies the numerical curves show a gap with the experimental data up to 10 dB. However, the numerical results can be considered reliable in the frequency range where human hearing is most sensitive [83].

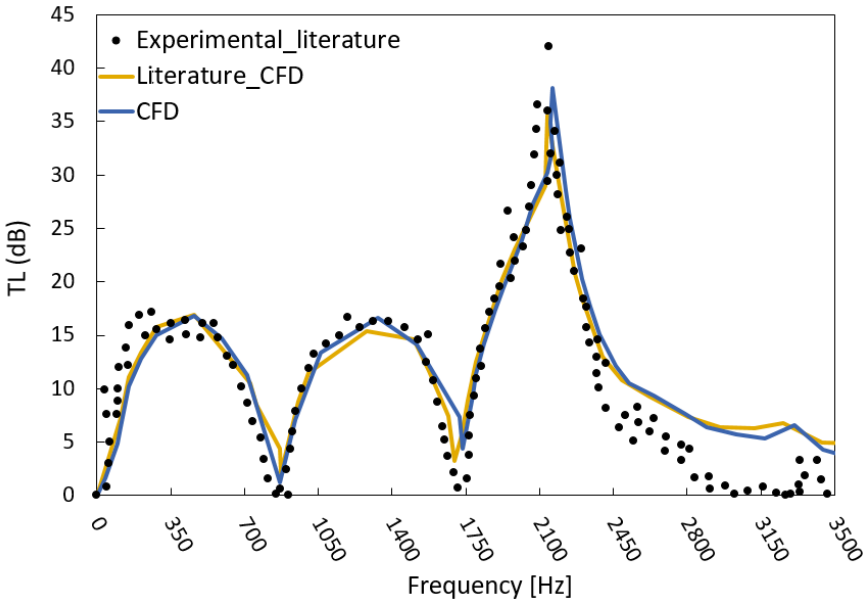

Figure A5-III: Comparison between literature and calculated TL.

Appendix 6

Experimental Measurements on a Marine Diesel Genset Mockup

A mockup employed to investigate chemical emission, vibration and noise generated by a marine engine has been mounted in a laboratory of the University of Trieste.
The mockup (Figure A6-I) is composed of a 4 stroke Genset engine Iveco with the characteristics reported in Table A6-I, mounted on a foundation and with a modular exhaust line that allows for testing different components in different configurations.

Table A6-I: 4 stroke Genset Iveco characteristics.

Engine model	N. of cylinders	Bore x Stroke [mm]	RPM
8361SRi26	6 in-line	115 x 130	1500

Figure A6-I: Experimental mockup.

First of all, the engine target frequencies have to be evaluated, as the TL of exhaust line components has to be optimized in correspondence with that values and, even more important, the transparent frequency of the TLs must not coincide with the engine frequencies. The exhaust noise spectrum always contains strong tones associated with the

rate of cylinder firings. The lowest tone is the CFR (Cylinder Frequency Rate), which is the firing rate for every single cylinder, while the EFR (Engine Firing Rate) is generally the strongest tone in the exhaust spectrum. For a 4 stroke engine CFR and EFR can be expressed in the following form [86]:

$$CFR = {RPM}/{120} \qquad \textbf{Eq. A6-I}$$

$$EFR = CFR \cdot N_c \qquad \textbf{Eq. A6-II}$$

where N_c is the number of cylinders. To obtain higher-order harmonics of CFR and EFR is sufficient to multiply their value for the number of desired harmonics. In general, harmonics since the 4th order are considered for TL optimization, as higher-order harmonics do not significantly influence exhaust gas noise [87].

Table A6-II reports the EFR up to the 4th order for the Genset I, while Figure A6-II highlights the EFR measured on the Genset; a good fitting between the frequencies of the engine harmonics can be observed. In Figure A6-II the other pecks represent the CFRs, in Table A6-III the first five values are reported.

Table A6-II: Genset Iveco EFRs.

Orders	**1th**	**2th**	**3th**	**4th**
EFR [Hz]	75	150	225	300

Table A6-III: Genset Iveco CFRs.

Orders	**1th**	**2th**	**3th**	**4th**	**5th**
CFR [Hz]	12.5	25.0	37.5	50.0	62.5

Appendix 6

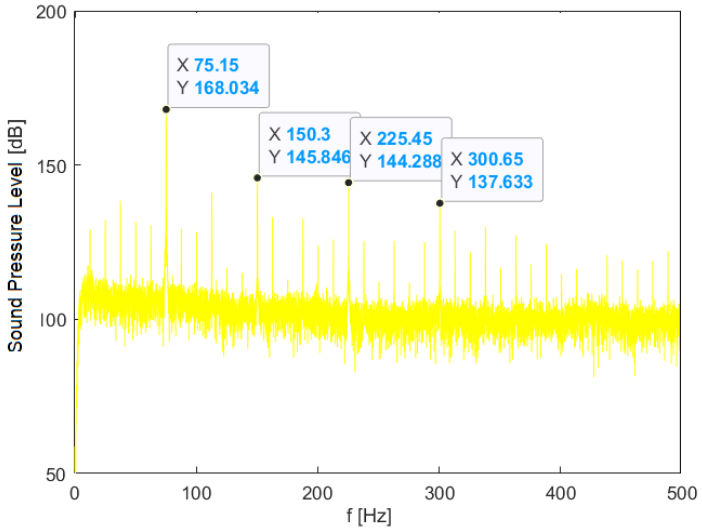

Figure A6-II: Narrow band sound pressure level.

In the presented study, the mockup is used to measure the TL of a DOC (Figure A3-VI) and the flow conditions at the inlet and the outlet. Flow conditions are needed to properly elaborate the registered signals to calculate the TL, as well as for CFD modelling settings and comparison (see Chapter 4).

The TL is obtained applying the two-loads techniques (Chapter 2), using as loads the open-end and the standard silencer of the Genset (Figure A6-III). Four microphone locations are considered, two before and two after the DOC (Figure A6-III), with a spacing of 300 mm and a distance from the flanges of at least 2 diameters of the exhaust pipe [88]. The probe spacing is selected based on the maximum considered frequency [49,88] that in this case is 500 Hz, as the 4th order of the EFR is at 300 Hz (Table A6-II). Two different types of microphones are used for the measurements: Kistler Piezoresistive Absolute Pressure Sensors PiezoSmart® 4045A and GRAS 40SC CCP Probe Microphone. The two sensors have different characteristics and potentials (e.g., sensitivity, frequency range, ease of breaking during tests), further studies have to be performed in future to compare and optimize the probes for in-duct measurements of exhaust gas noise.

Appendix 6

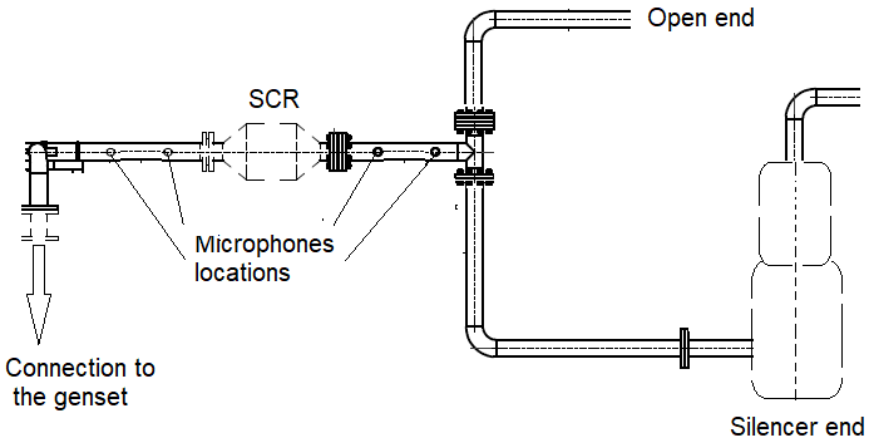

Figure A6-III: Configuration of exhaust line for the two-load technique.

Flow characteristics are measured with a Flowtest ST made by TCR Tecora, which combines a Pitot tube with a thermocouple. The probe is inserted in the same locations as microphones, to a depth such as to measure the center of the exhaust pipe. Three measures are performed for each measuring point and the values averaged over a period of 5 min are reported in **Error! Reference source not found.** A6-IV.

Table A6-IV: Averaged flow conditions.

Configuration	Location	Mean Temperature [°C]	Mean Velocity [m/s]	Mean Relative Pressure [Pa]
Open-end	In	269.0	44.2	1270
	Out	272.8	42.8	710
Silencer end	In	270.0	43.3	1386
	Out	268.8	41.5	812

Figure A6-IV reports the comparison between the numerical TL (see Chapter 4) and the measured TL, obtained by processing the time domain signals acquired with the microphones with a Matlab code that implement the two load-technique (Chapter 2).

Appendix 6

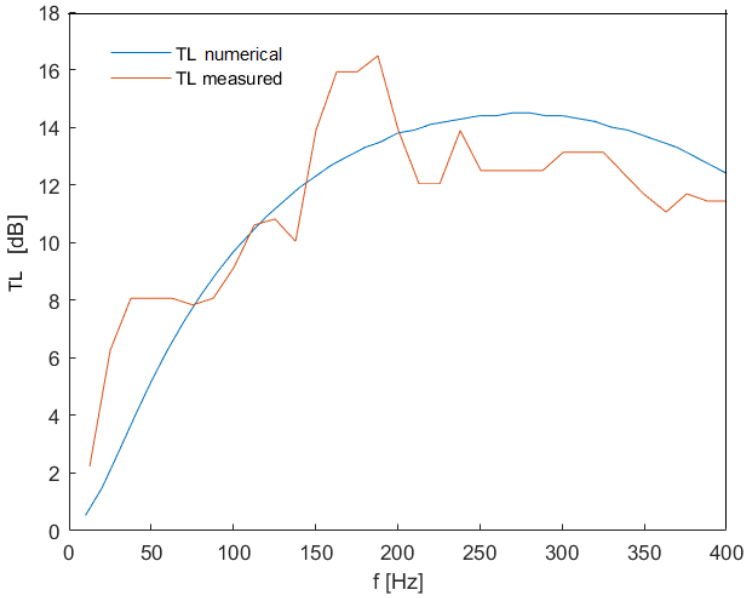

Figure A6-IV: Numerical *vs* measured TL of DOC with flow.

References

1. Fratila (Adam), A.; Gavril (Moldovan), I.A.; Nita, S.C.; Hrebenciuc, A. The Importance of Maritime Transport for Economic Growth in the European Union: A Panel Data Analysis. *Sustainability* **2021**, *13*, 7961, doi:10.3390/su13147961.

2. IMO *Revised MARPOL Annex VI*; 2008;

3. Chen, Y.; Lv, L. Design and Evaluation of an Integrated SCR and Exhaust Muffler from Marine Diesels. *J. Mar. Sci. Technol.* **2015**, *20*, 505–519, doi:10.1007/s00773-014-0302-1.

4. Ushakov, S.; Stenersen, D.; Einang, P.M.; Ask, T.Ø. Meeting Future Emission Regulation at Sea by Combining Low-Pressure EGR and Seawater Scrubbing. *J. Mar. Sci. Technol. Jpn.* **2020**, *25*, 482–497, doi:10.1007/s00773-019-00655-y.

5. Zhao, Y.; Fan, Y.; Fagerholt, K.; Zhou, J. Reducing Sulfur and Nitrogen Emissions in Shipping Economically. *Transp. Res. Part Transp. Environ.* **2021**, *90*, 102641, doi:https://doi.org/10.1016/j.trd.2020.102641.

6. Johnsen, K.; Kock, F.; Strøm, A.; Chryssakis, C. *Global Sulphur Cap 2020 Update*; https://www.dnvgl.com/maritime/publications/global-sulphur-cap-2020.html, 2019; p. 52;.

7. Oil Price Information Available online: https://www.petrolbunkering.com/price-information/ (accessed on 22 February 2021).

8. Https://Shipandbunker.Com/Prices/Emea/Nwe/Nl-Rtm-Rotterdam#IFO380, Accessed on June 3rd.

9. Lindstad, H.E.; Rehn, C.F.; Eskeland, G.S. Sulphur Abatement Globally in Maritime Shipping. *Transp. Res. Part Transp. Environ.* **2017**, *57*, 303–313, doi:10.1016/j.trd.2017.09.028.

10. Https://Www.Wartsila.Com/Media/News/22-09-2020-Scrubbers-Shown-to-Have-Lower-Climate-Impact-than-Low-Sulphur-Fuel-2786812 2020.

11. Exhaust Gas Scrubber Washwater Effluent. 46.

12. Boscarato, I.; Hickey, N.; Kašpar, J.; Prati, M.V.; Mariani, A. Green Shipping: Marine Engine Pollution Abatement Using a Combined Catalyst/Seawater Scrubber System. 1. Effect of Catalyst. *J. Catal.* **2015**, *328*, 248–257, doi:10.1016/j.jcat.2014.12.013.

13. IMO *RESOLUTION MSC.337(91), CODE ON NOISE LEVELS ON BOARD SHIPS*; 2012;

14. Loyd's Register Procedure for the Determination of Airborne Noise Emissions from Marine Vessels 2019.

15. European Committee for Standardization *Directive 2006/87 - 2006/87/EC Directive of the European Parliament and of the Council of 12 December 2006 Laying down Technical Requirements for Inland Waterway Vessels*; 2006;

16. Wartsila spa Https://Cdn.Wartsila.Com/Docs/Default-Source/Product-Files/Egc/Brochure-o-Env-Wartsila-Nox-Reducer.Pdf.

17. Denia, F.D.; Martínez-Casas, J.; Carballeira, J.; Nadal, E.; Fuenmayor, F.J. Computational Performance of Analytical Methods for the Acoustic Modelling of Automotive Exhaust Devices Incorporating Monoliths. *J. Comput. Appl. Math.* **2018**, *330*, 995–1006, doi:10.1016/j.cam.2017.03.010.

18. Sridhara, B.S.; Crocker, M.J. Review of Theoretical and Experimental Aspects of Acoustical Modeling of Engine Exhaust Systems. *J. Acoust. Soc. Am.* **1994**, *95*, 2363–2370, doi:10.1121/1.408746.

19. Tao, Z.; Seybert, A.F. A Review of Current Techniques for Measuring Muffler Transmission Loss.; May 5 2003; pp. 2003-01–1653.

20. Selvakumar, K.; Kim, M.Y. A Numerical Study on the Fluid Flow and Thermal Characteristics inside the Scrubber with Water Injection. *J. Mech. Sci. Technol.* **2016**, *30*, 915–923, doi:10.1007/s12206-016-0145-2.

21. Fan, W.; Guo, L.-X. An Investigation of Acoustic Attenuation Performance of Silencers with Mean Flow Based on Three-Dimensional Numerical Simulation. *Shock Vib.* **2016**, *2016*, 1–12, doi:10.1155/2016/6797593.

22. Kalita, U.; Singh, D.M. Design and CFD Analysis on Flow through a Reactive Muffler of Four-Cylinder Diesel Engine. 13.

23. Bilawchuk, S.; Fyfe, K.R. Comparison and Implementation of the Various Numerical Methods Used for Calculating Transmission Loss in Silencer Systems. *Appl. Acoust.* **2003**, *64*, 903–916, doi:10.1016/S0003-682X(03)00046-X.

24. Jeon, S.; Kim, D.; Hong, C.; Jeong, W. Acoustic Performance of Industrial Mufflers with CAE Modeling and Simulation. *Int. J. Nav. Archit. Ocean Eng.* **2014**, *6*, 935–946, doi:10.2478/IJNAOE-2013-0223.

25. Fu, J.; Xu, M.; Zheng, W.; Zhang, Z.; He, Y. Effects of Structural Parameters on Transmission Loss of Diesel Engine Muffler and Analysis of Prominent Structural Parameters. *Appl. Acoust.* **2021**, *173*, 107686, doi:10.1016/j.apacoust.2020.107686.

26. Swamy, M.; Kulkarni, R.; Dharmadhikari, R.; Rajput, S. Estimation of Pressure Drop across Exhaust System by CFD Simulation. **2020**, *07*, 7.

27. Liu, L.; Zheng, X.; Hao, Z.; Qiu, Y. A Time-Domain Simulation Method to Predict Insertion Loss of a Dissipative Muffler with Exhaust Flow. *Phys. Fluids* **2021**, *33*, 067114, doi:10.1063/5.0056316.

28. Zhu, D.D.; Ji, Z.L. Transmission Loss Prediction of Reactive Silencers Using 3-D Time-Domain CFD Approach and Plane Wave Decomposition Technique. *Appl. Acoust.* **2016**, *112*, 25–31, doi:10.1016/j.apacoust.2016.05.004.

29. Kyaw Oo D'Amore, G.; Mauro, F. Numerical Study on Modelling Perforated Elements Using Porous Baffle Interface and Porous Region. *J. Eng. Des. Technol.* **2021**, doi:10.1108/JEDT-07-2021-0356.

30. Gardner, B.; Mejdi, A.; Musser, C.; Chaigne, S.; De Campos Macarios, T. Coupled CFD and Vibro-Acoustic Modeling of Complex-Shaped Mufflers Accounting for Non-Uniform Mean Flow Effects.; June 15 2015; pp. 2015-01–2313.

31. Kašpar, J.; Fornasiero, P.; Hickey, N. Automotive Catalytic Converters: Current Status and Some Perspectives. *Catal. Today* **2003**, *77*, 419–449, doi:10.1016/S0920-5861(02)00384-X.

32. Zhang, Q.; Wu, Y.; Yuan, H. Recycling Strategies of Spent V2O5-WO3/TiO2 Catalyst: A Review. *Resour. Conserv. Recycl.* **2020**, *161*, doi:10.1016/j.resconrec.2020.104983.

33. Sung, Y.; Choi, M.; Park, T.; Choi, C.; Park, Y.; Choi, G. Synergistic Effect of Mixer and Mixing Chamber on Flow Mixing and NOx Reduction in a Marine Urea-SCR System. *Chem. Eng. Process. - Process Intensif.* **2020**, *150*, 107888, doi:10.1016/j.cep.2020.107888.

34. Jang, J.; Na, S.; Roh, H.; Ahn, S.; Choi, G. Spraying and Mixing Characteristics of Urea in a Static Mixer Applied Marine SCR System. *Energies* **2021**, *14*, 5788, doi:10.3390/en14185788.

35. Konstandopoulos, A.G.; Zarvalis, D.; Chasapidis, L.; Deloglou, D.; Vlachos, N.; Kotrba, A.; Anderson, G. Investigation of SCR Catalysts for Marine Diesel Applications. *SAE Int. J. Engines* **2017**, *10*, 1653–1666, doi:10.4271/2017-01-0947.

36. Zhang, G.; Yan, H.; Li, T.; Zhu, Y.; Zhou, S.; Feng, Y.; Zhou, W. Relation Analysis on Emission Control and Economic Cost of SCR System for Marine Diesels. *Sci. Total Environ.* **2021**, *788*, 147856, doi:10.1016/j.scitotenv.2021.147856.

37.Https://Www.Yanmar.Com/Global/about/Technology/Technical_review/2018/0413_2.Html.

38. Exhaus Gas Cleaning System Association *EGCSA Handbook 2012 - A Practical Guide to Exhaust Gas Cleaning Systems for the Maritime Industry*; 2012;

39. Gerald T. Joseph; David S. Beachler *Scrubber Systems Operation Review*; Environmental Programs;

40. United States Environmental Protection Agency Office of Wastewater Management Washington, DC 20460 *Exhaust Gas Scrubber Washwater Effluent*; 2011;

41. Bodn, H.; Glav, R. Exhaust and Intake Noise and Acoustical Design of Mufflers and Silencers. In *Handbook of Noise and Vibration Control*; Crocker, M.J., Ed.; John Wiley & Sons, Inc.: Hoboken, NJ, USA, 2007; pp. 1034–1053 ISBN 978-0-470-20970-7.

42. Munjal, M.L. *Acoustics of Ducts and Mufflers*; 2nd ed.; John Wiley & Sons, Ltd: Chichester, United Kingdom, 2014; ISBN 978-1-118-44312-5.

43. Beranek L.L. and Ver I.L. Noise and Vibration Control Engineering 1992.

44. Chung, J.Y.; Blaser, D.A. Transfer Function Method of Measuring In-duct Acoustic Properties. II. Experiment. *J. Acoust. Soc. Am.* **1980**, *68*, 914–921, doi:10.1121/1.384779.

45. Chung, J.Y.; Blaser, D.A. Transfer Function Method of Measuring In-duct Acoustic Properties. I. Theory. *J. Acoust. Soc. Am.* **1980**, *68*, 907–913, doi:10.1121/1.384778.

46. Munjal, M.L.; Doige, A.G. Theory of a Two Source-Location Method for Direct Experimental Evaluation of the Four-Pole Parametersof an Acoustic Element. *J. Sound Vib.* **1990**, *141(2)*, 323–333.

47. Finite Element Method for Acoustics. 55.

48. Antebas, A.G.; Denia, F.D.; Pedrosa, A.M.; Fuenmayor, F.J. A Finite Element Approach for the Acoustic Modeling of Perforated Dissipative Mufflers with Non-Homogeneous Properties. *Math. Comput. Model.* **2013**, *57*, 1970–1978, doi:10.1016/j.mcm.2012.01.021.

49. ISO *10534-2- Determination of Sound Absorption Coefficient and Impedance in Impedances Tubes - Part 2: Transfer Function Method*; 2001;

50. Hexagon, FFT *Actran 2020 User's Guide Vol. 1 Installation, Operations, Theory and Utilities*; 2020th ed.; 2020;

51. Maa, D.-Y. Potential of Microperforated Panel Absorber. 6.

52. Chen, Z.; Ji, Z.; Huang, H. Acoustic Impedance of Perforated Plates in the Presence of Fully Developed Grazing Flow. *J. Sound Vib.* **2020**, *485*, 115547, doi:10.1016/j.jsv.2020.115547.

53. Lawn, C. The Acoustic Impedance of Perforated Plates under Various Flow Conditions Relating to Combustion Chamber Liners. *Appl. Acoust.* **2016**, *106*, 144–154, doi:10.1016/j.apacoust.2016.01.005.

54. Chen, Z.; Ji, Z.; Huang, H. Acoustic Impedance of Perforated Plates in the Presence of Bias Flow. *J. Sound Vib.* **2019**, *446*, 159–175, doi:10.1016/j.jsv.2019.01.031.

55. Carcione, J.M. *Wave Fields in Real Media: Wave Propagation in Anisotropic, Anelastic, Porous and Electromagnetic Media*; Handbook of geophysical exploration. Seismic exploration; Elsevier: Amsterdam Boston [etc.], 2015; ISBN 978-0-08-099999-9.

56. Loudon, C.; McCulloh, K. Application of the Hagen—Poiseuille Equation to Fluid Feeding through Short Tubes. *Ann. Entomol. Soc. Am.* **1999**, *92*, 153–158, doi:10.1093/aesa/92.1.153.

57. Beltman, W.M. VISCOTHERMAL WAVE PROPAGATION INCLUDING ACOUSTO-ELASTIC INTERACTION, PART I: THEORY. *J. Sound Vib.* **1999**, *227*, 555–586, doi:10.1006/jsvi.1999.2355.

58. Sambuc, C.; Lielens, G.; Coyette, J.-P. An Extension of the Low Reduced Frequency Model for Viscothermal Acoustic Propagation Within Waveguides. In Proceedings of the ASME 2012 Noise Control and Acoustics Division Conference; American Society of Mechanical Engineers: New York City, New York, USA, August 19 2012; pp. 285–290.

59. Gianni Comini; Giulio Croce; Enrico Nobile *Fondamenti Di Termofluidodinamica Computazionale*; 4°.; S.G.E.; ISBN 88-89884-29-0.

60. Katz, B.F.G. Method to Resolve Microphone and Sample Location Errors in the Two-Microphone Duct Measurement Method. *J. Acoust. Soc. Am.* **2000**, *108*, 2231–2237, doi:10.1121/1.1314318.

61. Brigham, E.O. *The Fast Fourier Transform and Its Applications*; Prentice-Hall signal processing series; Prentice Hall: Englewood Cliffs, N.J, 1988; ISBN 978-0-13-307505-2.

62. Kizilaslan, M.A.; Demirel, E.; Aral, M.M. Effect of Porous Baffles on the Energy Performance of Contact Tanks in Water Treatment. *Water* **2018**, *10*, 1084, doi:10.3390/w10081084.

63. Giada Kyaw Oo D'Amore; Mitja Morgut; Francesco auro; Giovanni Rognoni; Marco Biot A Combined CFD-FEM Approach to Evaluate Acoustic Performances of an Integrated Scrubber-Silencer for Marine Applications.; June 17 2022.

64. Bailly, C.; Juve, D. A Stochastic Approach to Compute Subsonic Noise Using Linearized Euler's Equations. In Proceedings of the 5th AIAA/CEAS Aeroacoustics Conference and Exhibit; American Institute of Aeronautics and Astronautics: Bellevue,WA,U.S.A., May 10 1999.

65. M. J. L ighthill On Sound Generated Aerodynamically I. General Theory. 24.

66. Mohring, W. A Well Posed Acoustic Analogy Based on a Moving Acoustic Medium. *ArXiv10093766 Phys.* **2010**.

67. Zhang, H.; Fan, W.; Guo, L.-X. A CFD Results-Based Approach to Investigating Acoustic Attenuation Performance and Pressure Loss of Car Perforated Tube Silencers. *Appl. Sci.* **2018**, *8*, 545, doi:10.3390/app8040545.

68. Ennio Macchi; Marco Astolfi *Organic Rankine Cycle (ORC) Power Systems-Chapter 13-Heat Transfer and Heat Exchangers*; Woodhead Publishing.; 2017; ISBN 978-0-08-100510-1.

69. Mauro, F.; Braidotti, L.; Trincas, G. A Model for Intact and Damage Stability Evaluation of CNG Ships during the Concept Design Stage. *J. Mar. Sci. Eng.* **2019**, *7*, 450, doi:10.3390/jmse7120450.

70. Harrell, F. *Regression Modelling Strategies: With Application to Linear Models, Logistic Regression, and Survival Analysis*; Springer-Verlag: New York, NY, USA, 2001;

71. Panigrahi, S.N.; Munjal, M.L. Backpressure Considerations in Designing of Cross Flow Perforated-Element Reactive Silencers. *Noise Control Eng. J.* **2007**, *55*, 504, doi:10.3397/1.2817808.

72. Kwaśniewski, L. Application of Grid Convergence Index in FE Computation. *Bull. Pol. Acad. Sci. Tech. Sci.* **2013**, *61*, doi:10.2478/bpasts-2013-0010.

73. Star-CCM+ 2020.2 User Manual.

74. Kyaw Oo D'Amore, G.; Morgut, M.; Biot, M.; Mauro, F. Numerical Study on the Influence of Porous Baffle Interface and Mesh Typology on the Silencer Flow Analysis. *Mar. Syst. Ocean Technol.* **2022**, doi:10.1007/s40868-022-00114-1.

75. Berg, A. Numerical and Experimental Study of the Fluid Flow in Porous Medium in Charging Process of Stratified Thermal Storage Tank. Master of Science Thesis, KTH School of Industrial Engineering and Management Energy Technology: STOCKHOLM, 2013.

76. Innocentini, M.D.M.; Salvini, V.R.; Macedo, A.; Pandolfelli, V.C. Prediction of Ceramic Foams Permeability Using Ergun's Equation. *Mater. Res.* **1999**, *2*, 283–289, doi:10.1590/S1516-14391999000400008.

77. Tan, W.-H.; Ripin, Z.M. 973. Analysis of Exhaust Muffler with Micro-Perforated Panel. . *VOLUME 15*, 17.

78. Katz, B.F.G. Method to Resolve Microphone and Sample Location Errors in the Two-Microphone Duct Measurement Method. *J. Acoust. Soc. Am.* **2000**, *108*, 2231–2237, doi:10.1121/1.1314318.

79. Kyaw Oo D'Amore, G.; Biot, M.; Mauro, F.; Kašpar, J. Green Shipping—Multifunctional Marine Scrubbers for Emission Control: Silencing Effect. *Appl. Sci.* **2021**, *11*, doi:10.3390/app11199079.

80. *Computational Acoustics of Noise Propagation in Fluids: Finite and Boundary Element Methods*; Marburg, S., Nolte, B., Eds.; Springer: Berlin, 2008; ISBN 978-3-540-77447-1.

81. Marburg, S. SIX BOUNDARY ELEMENTS PER WAVELENGTH: IS THAT ENOUGH? 28.

82. Yang, Y.; Jia, H.; Lu, W.; Sun, Z.; Yang, J. Impedance-Matching Acoustic Bend Composed of Perforated Plates and Side Pipes. *J. Appl. Phys.* **2017**, *122*, 054502, doi:10.1063/1.4996848.

83. Dubno, J.R.; Eckert, M.A.; Lee, F.-S.; Matthews, L.J.; Schmiedt, R.A. Classifying Human Audiometric Phenotypes of Age-Related Hearing Loss from Animal Models. *J. Assoc. Res. Otolaryngol.* **2013**, *14*, 687–701, doi:10.1007/s10162-013-0396-x.

84. Https://Www.Engineeringtoolbox.Com/Dry-Air-Properties-D_973.Html 2021.

85. Giada KYAW OO D'AMORE; Francesco MAURO; Giovanni ROGNONI; Mitja MORGUT; Marco BIOT A Combined CFD-FEM Approach to Evaluate Acoustic Performances of an Integrated Scrubber-Silencer for Marine Applications.; Genoa-La Spezia (Italy), June 15 2022.

86. Rao, P.C.; Varma, B.M. Muffler Design, Development and Validation Methods. **2007**, *5*, 14.

87. Shah, S.; Kuppili, S.; Hatti, K.; Thombare, D. A Practical Approach towards Muffler Design, Development and Prototype Validation.; September 28 2010; pp. 2010-32–0021.

88. Paolo Bonfiglio, Materiacustica Personal Comunications.